Statistical study of subauroral arc detachment at Athabasca, Canada: new insights on STEVE

Sneha Yadav[1], Kazuo Shiokawa[1], Yuichi Otsuka[2], and Martin Connors[3]

[1]Institute for Space-Earth Environmental Research, Nagoya University
[2]Nagoya University
[3]Athabasca University

November 25, 2022

Abstract

We present the first comparative statistical study of subauroral arc detachment from the main auroral oval at Athabasca (magnetic latitude = 61.5°N), Canada, for three different types of subauroral arcs: pure red arc, red arc with simultaneous emission in green-line (red+green arc), and STEVE (strong thermal emission velocity enhancement). Based on 15-years (2006-2020) of all-sky imaging observations, this study not only uncovers the occurrence characteristics of different arcs but also provides important insights into the specific geomagnetic conditions under which STEVE develops. Red arc was the most common subauroral arc (139 events), followed by red+green arc (42 events), and STEVE (26 events) was a rare phenomenon. The detachment rate of red and red+green arcs exhibits dependence on both the solar flux and geomagnetic activity. The detachment rate of STEVE was higher during premidnight, whereas red and red+green arcs were higher around the midnight sector. The geomagnetic activity was relatively higher for STEVE, the decrease in the AL index and local X-component magnetic variations were ˜2-3 times higher for STEVE as compared to other arcs. STEVE shows a strong association with asymmetric ring current in terms of prominent bay-like enhancement in ASY-H index prior to the STEVE detachment. Such bay-like enhancement was ˜4 times higher for STEVE as compared to other arcs. STEVE events were accompanied by dispersionless injection for both electron and proton flux at the geosynchronous orbit. These results unambiguously suggest that STEVE develops after the substorm associated energy injection and significant intensification of asymmetric ring current.

1 Introduction

The subauroral ionosphere is the region where magnetic field changes from stretched to more dipolar field like topology. The nightside poleward part of the subauroral ionosphere is affected by electron precipitation from the plasma sheet, whereas the equatorward part is maintained by plasma from the plasmasphere. The ring current is the energy source for the magnetospheric electron heat flux in the subauroral region (e.g. Hoch, 1973; Rees and Roble, 1975; Kozyra et al., 1987). During geomagnetically disturbed intervals, the heated electrons, generated by the interaction between plasmasphere and ring current, fall into the ionosphere at subauroral latitudes along magnetic field lines. Further, the strong poleward electric field located equatorward of the auroral oval produces latitudinally narrow regions of duskward plasma flow at subauroral latitudes known as polarization jet (Galperin et al., 1974) or SAID (subauroral ion drifts) (Smiddy et al., 1977; Spiro et al., 1979). Thus, the subauroral ionosphere experiences a number of highly dynamic processes related to convection electric field, coupling of trapped energetic particles, and thermal plasma, causing the formation of various types of optical features in this region (e.g., Frey, 2007, for a review). One of the most fascinating optical features observed at the subauroral ionosphere is the 'subauroral arc'. Unlike typical auroral arcs, the subauroral arcs may not be always caused by direct excitation from energetic particle precipitation (e.g., Gallardo-Lacourt et al. 2021, for a review).

Stable auroral red (SAR) arcs are most common type of subauroral arc and have been studied extensively since their discovery in the 1950s (Barbier, 1958). The red-line emissions of SAR arcs are caused by the interaction of the inner edge of the ring current with the contracted plasmasphere. The Coulomb collision is considered as a main mechanism through which energy is transferred from ring current ions (several tens of keV) to plasmaspheric electrons (energies less than 1 eV) (Cole, 1965; Kozyra et al., 1987). Energized thermal electrons can transport energy down to the ionosphere via heat conduction or as a low-energy electron flux (e.g., Cole, 1965), exciting atomic oxygen to the O(^{1}D) state. SAR arcs with weak green-line (557.7 nm) emission have been reported by past studies (e.g., Mendillo et al., 2016; Inaba et al., 2021). A newly recognized subauroral optical structure, known as STEVE (strong thermal emission velocity enhancement), has also grasped the attention of the space physics community in recent years (e.g., MacDonald et al., 2018). STEVE is a visible purple color arc, often occasionally accompanied by green ray structure at the lower altitudes, known as picket fence.

Similar to SAR arc, STEVE is shown to be associated with enhancement in temperature and westward ion drift (MacDonald et al., 2018). Both SAR arcs and STEVE have been reported to occur in the recovery phase of substorms (Takagi et al., 2018; Gallardo-Lacourt et al., 2018). They are generated at or just inside the plasmapause (Cornwall et al., 1971; Kozyra et al., 1997; Chu et al., 2019). Although STEVE shows some similarities to SAR arcs in terms of their location and occurrence, the two phenomena differ markedly from each other. While SAR arcs are subvisual, spectrally pure red-line emission with little or no green emission, and long-lived (10 hours or longer) (e.g. Nagy et al., 1970), purple STEVE is visible to the naked eye, latitudinally narrow, and short-lived (˜around one-hour) (Gallardo-Lacourt et al., 2018). Unlike that of monochromatic SAR arcs (only 630.0 nm), STEVE spectrum consists of a continuum spectrum spanning between ˜400 and 730 nm (Gillies et al., 2019).

Recent studies have shown that common feature of both SAR arcs and STEVE is equatorward arc detachment from the main auroral oval (e.g., Shiokawa et al., 1999; 2009; 2017; Takagi et al., 2018; Gallardo-Lacourt et al., 2018; Yadav et al. 2021a). Using an all-sky imager (ASI) at Athabasca, Takagi et al. (2018) and Yadav et al. (2021) reported that, initially, SAR arcs and STEVE arcs appeared very close to the main auroral oval. As time progressed, this arc separated itself from the oval and moved equatorward when the main oval returned to higher latitudes. This feature is referred as the "detachment of arc from the oval". Anger et al. (1978) and Moshupi et al. (1979) first used the term "detached arcs" to describe the arc-like auroral features equatorward of the auroral oval observed by the ISIS 2 satellite scanning photometer. The ISIS-2 detached arcs displayed emissions in 391.4 nm (N_2^+) and 557.7 nm with no emission enhancement in 630.0 nm and occurred in the afternoon sector, hence are referred as "afternoon detached arcs". The detached arcs in the midnight sector at the subauroral latitudes with emission in both red- and green line (red+green arc) have been shown to be associated with the low-energy particle precipitation from the plasma sheet (Yadav et al., 2021b; under communication). Detached proton arcs have also been observed in the subauroral region (Sakaguchi et al., 2008; Ozaki et al., 2021; Zhou et al., 2021; and reference therein). The proton arcs have been shown to be formed by the precipitation of high-energy ions caused by the interactions of electromagnetic ion cyclotron (EMIC) waves with ring current ions (e.g., Sakaguchi et al., 2008). On account of the generation mechanism of subauroral proton arcs, we have not considered protons arcs in the present study.

In the past, individual statistical study of SAR arc and STEVE have been carried out. For example, Gallardo-Lacourt et al. (2018) performed a statistical analysis for 28 STEVE events using Time History of Events and Macroscale Interactions during Substorms (THEMIS) all-sky imager and the Redline Emission Geospace Observatory (REGO) database that is, they performed the statistical analysis of STEVE using multiple sites. Based on 11 years of ASI observations at Athabasca, Takagi et al. (2018) performed a statistical analysis of detached SAR arc. Note that in the study of Takagi et al. (2018), weak 557.7-nm emission also accompanied the SAR arc for some cases. A statistical study of subauroral arc with simultaneous emission in red and green-line, hereafter referred as red+green arc, remains unexplored. A detailed comparative statistical study of geomagnetic conditions for different subauroral arcs at a single station is also missing from the literature. Here, we present a comparative statistical analysis on the detachment of red arcs, red+green arcs, and STEVE with reference to solar flux, geomagnetic activity, and magnetic local time (MLT) distribution. Such

a comparative study will not only enable disentangling the mysteries associated with STEVE, but also shed light on the specific geomagnetic conditions under which the arcs detached as red arc, red+green arc, and STEVE.

2 Database and methodology

One of the requirement to perform the statistical analysis is long-term availability of all-sky imaging observations for the arc detection. An OMTI (Optical Mesosphere Thermosphere Imager) (Shiokawa et al., 1999, 2009) all-sky imager (ASI) (camera no. 7) has been operating at Athabasca (54.6°N, 246.3°E, magnetic latitude: 61.5°N, L = 4.4), Canada, since September 3, 2005. Magnetic midnight for this ASI occurs at ˜8.1 UT. In the present study, we have used 15-years of continuous ASI observations from 2006-2020. The camera has a 180° field-of-view fish-eye lens, seven band-pass optical filters, and a thermoelectrically cooled CCD with 512 × 512 pixels. In order to increase the signal to noise ratio, CCD images are processed with 2 × 2 binning, so that the images had a resolution of 256 × 256 pixels. The seven band-pass filters of this camera allow measurement of airglow/auroral emissions at specific wavelengths: OI at 557.7 nm, OI at 630.0 nm, Hβ at 486.1 nm, Na at 589.3 nm, OH bands at 720–910 nm, OI at 844.6 nm, and nominal background at 572.5 nm. In this study, we have used images at all the wavelengths except for OH bands. The details about the exposure times of the images at different wavelengths are given in Yadav et al. (2021a).

The raw images are projected into the geographical latitude/longitude coordinates by assuming that the emission intensity has a peak at 250 km altitude for 630.0 nm and 120 km for the other wavelengths. We have constructed North-South (NS) keograms by stripping the slices of airglow images at the longitude of Athabasca (246.3°E). The keograms facilitate the study of temporal variations in the auroral emission intensities and their latitudinal motion.

As mentioned earlier, proton arcs are not considered in this study. Subauroral proton arcs, which exhibit emission in 557.7 nm, 630.0 nm, and 486.1 nm (Hβ), have been shown to occur simultaneously with Pc 1 geomagnetic pulsations in the frequency range of the EMIC wave (e.g., Sakaguchi et al., 2008). An induction magnetometer has been operating at Athabasca since September 2005. The induction magnetometer measures variation of a three-component geomagnetic field with a sensitivity of 0.45 (V/nT) at 6 Hz with a turnover frequency of 6 Hz. The dynamic magnetic field spectra used to decipher the presence of Pc 1 geomagnetic pulsations is available at the ISEE magnetometer website (https://stdb2.isee.nagoya-u.ac.jp/magne/induction/index.html). Detached red+green arcs with simultaneous occurrence of Pc 1 geomagnetic pulsation were eliminated from the present study.

To study the solar flux and geomagnetic activity dependence of detached arcs, we obtained the yearly solar flux and geomagnetic indices from the NASA's Space Physics Data Facility (SPDF) OMNI database. The 1-min resolution geomagnetic indices were also obtained from the OMNI database, used to examine the geomagnetic conditions during the detachment of arcs. The magnetometer data at Athabasca (ATHA), Fort Smith (FSMI; Lat 60.0°N, Long 248.2°N; magnetic latitude: 67.28°N), and Boulder (BOU; Lat 40.1°N, Long 254.7; magnetic latitude: 48.7°N) were used to access the substorm activity in the longitude zone of Athabasca ASI. Fort Smith is located in the auroral oval, whereas Boulder is a middle latitude station.

The magnetic field (MAG) and particle data from MAGnetospheric Electron Detector (MAGED) and MAGnetospheric Proton Detector (MAGPD) onboard Geostationary Operational Environmental Satellite (GOES) were used to identify the substorm injection signatures at the geosynchronous orbit. We used data from GOES-15 [135°W], GOES-14 [105°W], GOES-12 [75°W], and GOES-11 [135°W]. The GOES satellites were located between ˜19 to 24 MLT for all STEVE events. The longitudinal difference of GOES-15 and GOES-11 with Athabasca is ˜63 degree, whereas GOES-14 and GOES-12 is ˜38 degree and 8 degree, respectively. In this paper, we have shown only particle data from GOES-15 to demonstrate the dispersionless injection prior to three STEVE events occurring during 2018-2019.

We have used the Space Physics Environment Data Analysis Software (SPEDAS) tool (Angelopoulos et al., 2019) to download and analyze the 1-min geomagnetic activity indices, ground-based magnetic field, and GOES particle flux data. We used median subtracted X-component magnetograms in this study.

3 Observations

We used ASI images and N-S keogram to identify the detachment of arcs based on visual inspection. Figure 1 shows the typical ASI images at red-line (630.0 nm) and green-line (557.7 nm) for red arc (upper panel A), red+green arc (middle panel B), and STEVE (bottom panel C). Spectrally pure red-line emission is considered as red arcs, not associated with simultaneous observation in the green-line (panel A). The arc in red-line with simultaneous emission in green-line is referred as red+green arc (panel B). STEVE is a narrow bright arc compared to normal red arc, exhibiting wavy structure along the arc, and sometimes also picket fence structure in the green-line (panel C).

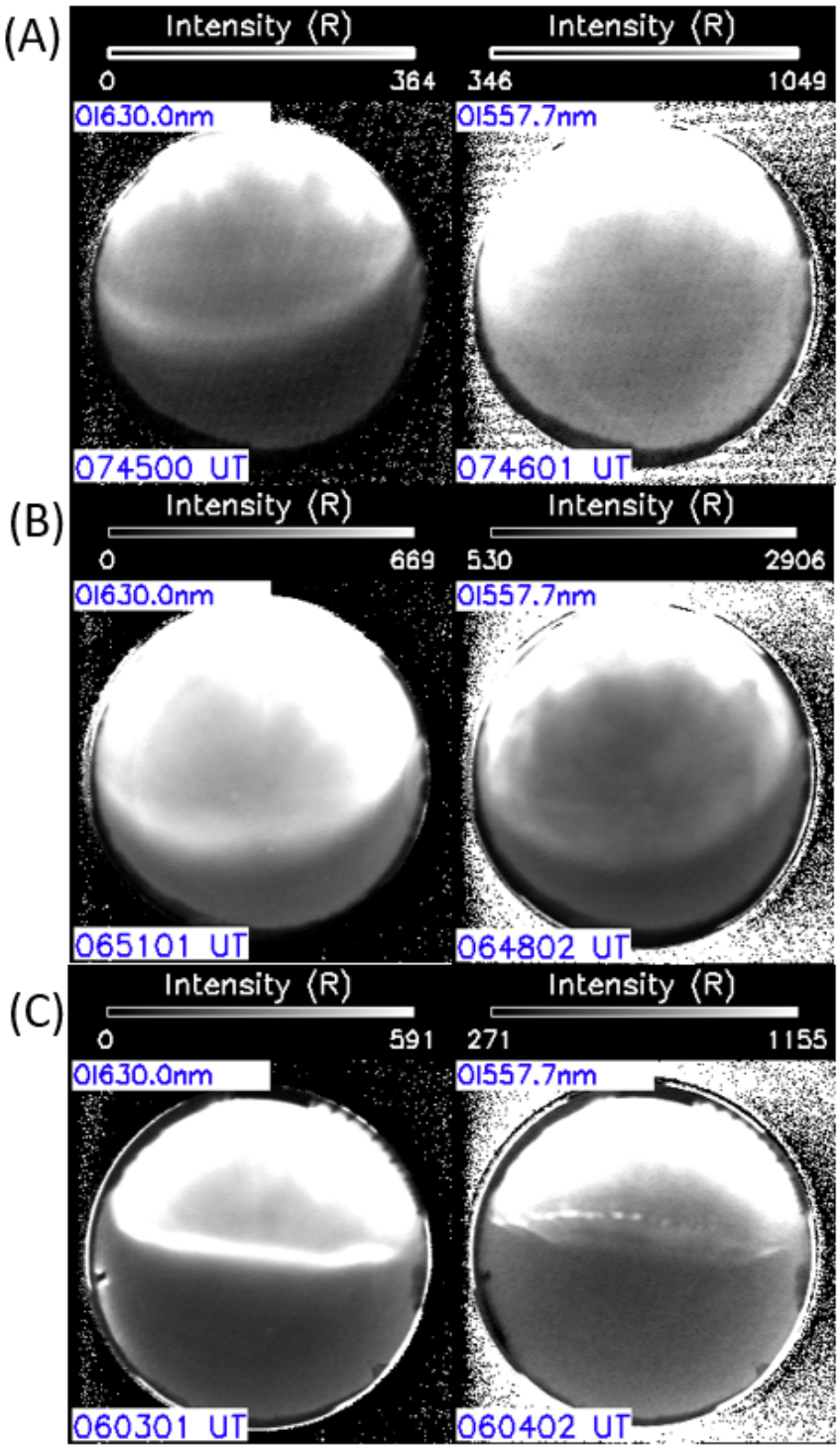

Figure 1: Typical all-sky images of red arc on September 17, 2017 (arc in 630.0 nm with no corresponding emission in 557.7 nm; upper panel A), red+green arc on May 14, 2015 (emission in both 630.0 nm and 557.7 nm; middle panel B), and STEVE on March 11, 2010 (bright arc in 630.0 nm and picket fence in 557.7 nm; bottom panel C).

Figure 2 shows a typical example of NS keogram for red-line (630.0 nm) and green-line (557.7 nm) for red arc (Event 1; upper panel A), red+green arc (Event 2; middle panel B), and STEVE (Event 3; bottom panel C). Before the detachment of all arcs, the high-latitude aurora expands equatorwards. When the oval aurora returned to higher latitudes, an arc detached itself from the main auroral oval and moved further equatorward. This phenomenon is referred as detachment of arc from the main auroral oval as described by Takagi et al. (2018) for SAR arc and Yadav et al. (2021a) for STEVE. For red arc (Event 1), this detachment was observed at ˜0740 UT in the red-line keogram. Although the equatorward extension of oval aurora is observed in the green-line keogram, arc detachment did not occur. For red+green arc (Event 2), the detachment of arc is observed in both the red-line and green-line keogram at ˜0645 UT. A narrow and bright arc structure detaching itself from the main auroral oval at ˜0615 UT is STEVE in the red-line (Event 3). By contrast, red arc appeared diffuse and wide (Event 1). For STEVE (Event 3), although 557.7 nm image shows the picket fence structure, the detachment of arc at ˜0615 UT is not observed, like in the red-line.

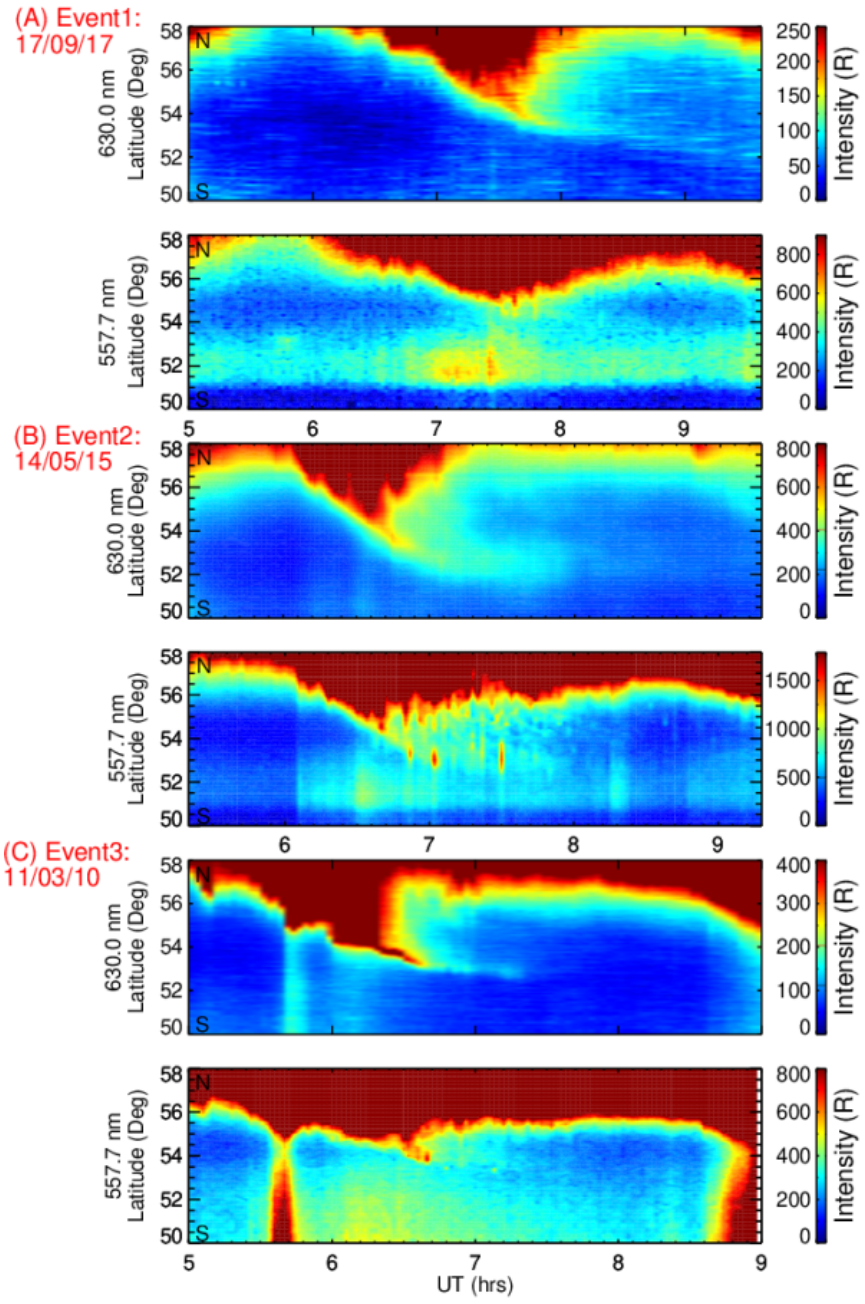

Figure 2: Typical NS keogram for red arc (Event 1), red+green arc (Event 2), and STEVE (Event 3).

For arc detachment statistics, first, the feature of arc detachment was identified from NS keograms by visual inspection. Then, we checked all-sky images to ensure that the features picked up from the keograms were east-west elongated arcs detaching from the main auroral oval. Only those arcs are considered which persisted at least 30 mins after their detachment from the main auroral oval. STEVE consists of continuum spectrum from 400-730 nm (Gilles et al., 2019). Therefore, although Figure 1 and 2 shows the STEVE emissions only in red- and green-line, the presence of STEVE is identified by using the images at all six filters including the "nominal background", except for the OH band, as described in Yadav et al. (2021a). The primary objective

of this study is to examine the detachment rate. So, cases in which detachment was not observed were not considered. Since STEVE is a rare event, we have considered STEVE events even when the detachment was ambiguous.

Given the fact that the ASI measurements have limitation as observations cannot be made if the sky is cloudy, only those nights are considered for which at least 4-hour observation was present. After this restriction, the number of nights available to us for identifying the arc detachment were reduced to 948. In 948 nights of observations and 6376 hours of data, we identified 139 red arcs, 42 red+green arc, and 26 STEVE events. Note that Takagi et al. (2018) analyzed the total occurrence (from the detachment until the arc remained detectable in the ASI images) of SAR (red) arcs, whereas the present study is focused solely on the detachment rate of red arcs, red+green arcs, and STEVE.

STEVE does not invariably display the feature of detachment from the main auroral oval. Occasionally, STEVE is found to emerge at the equatorward boundary of diffuse emissions that had already expanded equatorward from the main auroral oval. Out of 26 STEVE events, the detachment from the main auroral oval was observed for 13 events. For 4 events, the feature of detachment was not clear either because of the absence of images or presence of clouds. For the remaining 8 events, STEVE developed at the equatorward boundary of the intense diffuse emission that expanded equatorward from the main auroral oval. Two examples of such events are shown in supplementary Figure S1.

3.1 Statistics of detachment rate

The 'detachment of arc per hour' is defined as the ratio between total number of detachment events and total hours of data. Figure 3 shows the yearly (2006-2020) rate of detachment for red, red+green arcs, and STEVE. The yearly averaged variation of solar wind speed (Vx), Ap index, and F10.7 is superposed to study the association of arc detachment with the solar and geomagnetic activity. In general, the detachment rate of red+green arcs exhibits dependence on geomagnetic activity with higher detachment rate when Ap and solar wind speed were high and no occurrence for low Ap and solar wind speed years (2009-2011 and 2020). However, the detachment rate of both red and red+green arcs was low during 2016-2017 when the Ap index was the highest. Comparing the two solar minimum, the detachment rate of red arc was highest during 2018-2019 when both the solar wind and Ap index was at the higher levels as compared to 2008-2009. In comparison to red+green arcs, the detachment rate of red arcs was higher even for the lowest Ap years (2009-2010). These results suggest that the detachment rate of red and red+green arc exhibits dependence on both the geomagnetic activity (Ap and solar wind) and solar flux. The detachment of STEVE was maximum during the solar minimum year 2019, and then for 2010 and 2018. The high detachment rate of STEVE coincided with the high detachment rate of red arcs.

Figure 4 shows the detachment rate of red, red+green arcs, and STEVE as a function of MLT. The MLT distribution of detachment rate was calculated for each arc-type separately by dividing the total events observed in a particular 2-hour time slot to the total number of arc events. In general, the detachment rate of all arcs exhibits asymmetric distribution with highest rate in the premidnight sector. For STEVE, detachment rate is highest at 22-24 MLT, and then at 20-22 MLT, before midnight. The detachment rate of red and red+green arcs maximized around midnight, that is at 22-24 and 00-02 MLT.

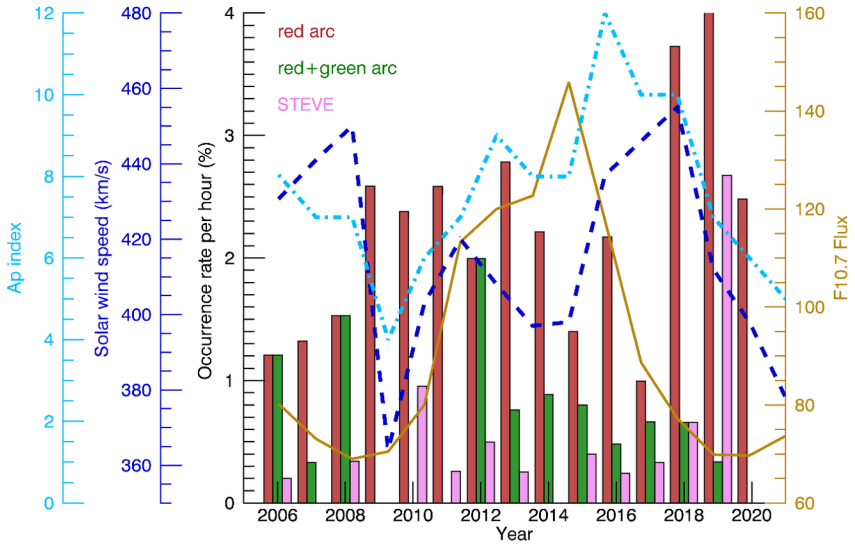

Figure 3: The yearly (2006-2020) variation of rate of detachment for red arc, red+green arc, and STEVE. Blue dashed, cyan dashed dot, and solid gold color curve represent the yearly averaged variation of solar wind speed (Vx), Ap index, and F10.7.

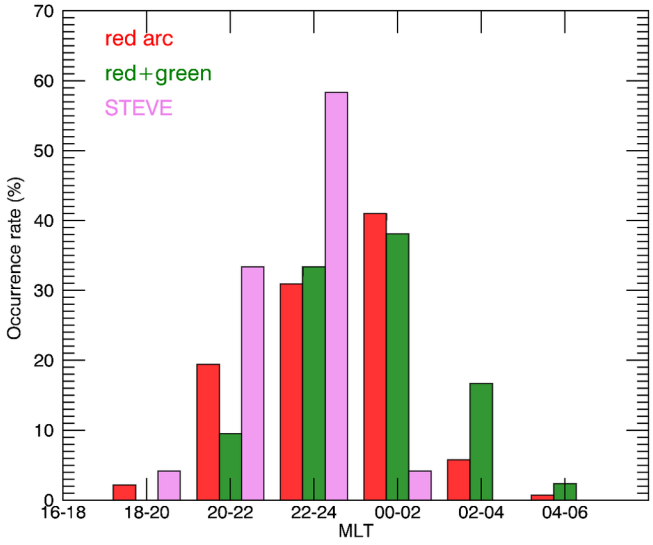

Figure 4: The detachment rate of red a rc, red+green arc, and STEVE as a function of MLT.

3.2 Superposed epoch analysis

In order to understand the specific geomagnetic activity during which subauroral arcs detached as red arc, red+green arc, and STEVE, we perform the superposed epoch analysis for different geomagnetic activity indices from 3 hr before to 3 hr after the detachment event. Note that the superposed epoch analysis of AL-index and SYM-H index for STEVE (Gallardo-Lacourt et al., 2018) and SAR arc (Takagi et al., 2018) has been already reported. These studies highlighted that both STEVE and SAR arc occurred at the end of expansion phase or just at the beginning of recovery phase. In the following subsections, we compare the results of superposed epoch analysis of different geomagnetic activity indices for three different types of arcs.

3.2.1 AL index

Figure 5 shows the results of superposed epoch analysis of AL index from 3 hr before to 3 hr after the detachment of (a) red arcs, (b) red+green arc, and (c) STEVE. The vertical dashed line at zero hour represents the time of detachment of arcs as detected in the optical data. The average values defined every 1-min for red arc, red+green arc, and STEVE are shown by red, green, and purple curve, respectively. The grey lines show the standard deviation. The AL index began to decrease ˜1 hr prior to the detachment of all arcs. Compared to the values 1-hr prior to the detachment, the AL-index exhibits a decrease of ˜ 250 nT for STEVE, ˜130 nT for red and red+green arc. The detachment of arcs occurred towards the end of expansion phase and beginning of recovery phase. Unlike red and red+green arc, the AL index for STEVE shows the presence of small perturbations around the end of expansion phase. In order to investigate this aspect in detail, we made the superposed epoch analysis using X-component magnetogram at FSMI, enable focusing on the detachment of arc with respect to auroral-zone substorm activity in the longitude of Athabasca ASI.

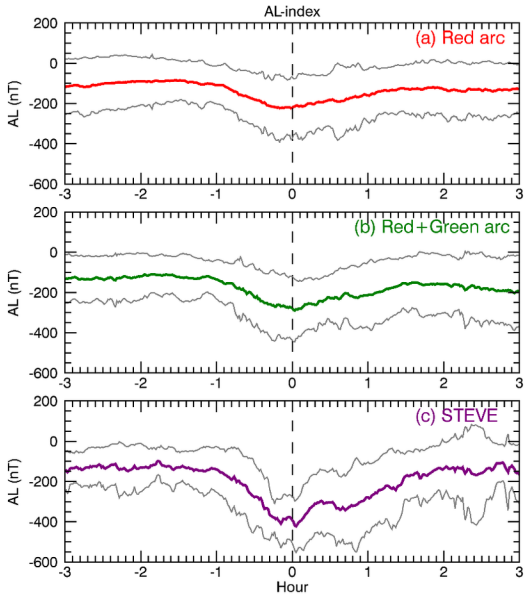

Figure 5: Superposed epoch analysis of (a) red arc (139 events), (b) red+green arc (42 events), and (c) STEVE (26 events). The vertical dashed line at zero hour represents the time of detachment of arcs as detected in the optical data. The average values defined every 1-min for red arc, red+green arc, and STEVE are shown by red, green, and purple curve, respectively. The grey lines show the standard deviation.

3.2.2 X-component magnetogram at Fort Smith

Figure 6 is same as Figure 5 but for X-component magnetogram at FSMI. In general, for all arcs, the X-component magnetic field at FSMI began to decrease 1 hr prior to the time of arc detachment, with its minimum value occurring around the detachment time. On average, the X-component magnetogram decreased ˜300 nT for STEVE, ˜200 nT for red+green arcs, and ˜100 nT for red arcs. The X-component magnetogram at FSMI displayed perturbations in the recovery phase of the substorms during STEVE detachment, not observed for other arcs. STEVE detachment coincided with a sharp recovery from the expansion phase and start of additional activity in the recovery phase of a substorm. By analyzing three STEVE events, Yadav et al. (2021) also reported the association of STEVE with additional activities in the recovery phase of a substorm by using X-component magnetogram at FSMI for three STEVE events.

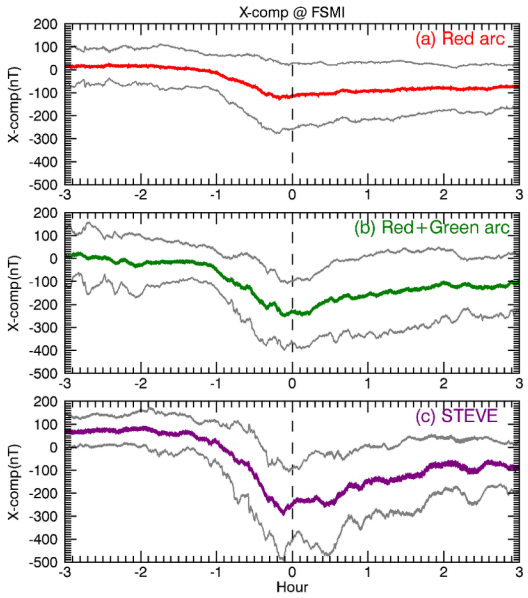

Figure 6: Same as Figure 5 but for X-component magnetogram at Fort Smith (FSMI).

3.2.3 X-component magnetogram at Athabasca

We also perform the superposed epoch analysis for the X-component magnetogram at Athabasca, shown in Figure 7. The X-component magnetogram at Athabasca began to decrease ˜1 hr before the detachment of red arc and red+green arc. For STEVE, X-component magnetogram at Athabasca showed a hump of slight (˜10 nT) enhancement ˜30-minutes prior to the detachment followed by a decrease. Such feature is not observed for red arc and red+green arc. The maximum decrease prior to detachment was ˜40 nT for STEVE and red+green arc and 20 nT for red arc.

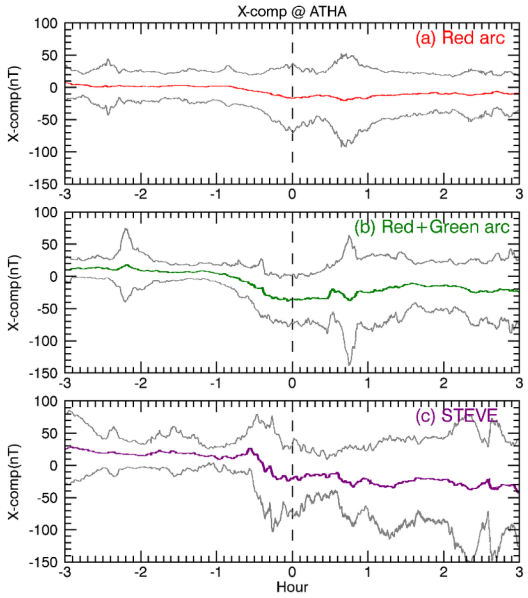

Figure 7: Same as Figure 5 but for X-component magnetogram at Athabasca (ATHA).

3.2.4 SYM-H index

Figure 8 shows the superposed epoch analysis for the SYM-H index. Takagi et al. (2018) reported no clear change in the SYM-H index before or after the detachment of SAR arcs. Similarly, the SYM-H index shows no change before and after the detachment of both red and red+green arcs. Unlike other arcs, the SYM-H index exhibits slight variations before and after the detachment of STEVE. The SYM-H index shows the hump of slight enhancement just prior to the detachment of STEVE. The hump is followed by a gradual decrease with the minimum values occurred 1 hr after the detachment of STEVE. The minimum value of the SYM-H index remains near -15 nT for red arcs, -20 nT for red+green arcs, and -25 nT for STEVE events. This indicates that STEVE likely to occur during relatively geomagnetically disturbed periods with more developed ring current as compared to red and red+green arcs.

3.2.5 ASY-H index

Figure 9 shows the superposed epoch analysis for the ASY-H index. In general, the ASY-H index began to increase gradually ˜1 hour before the arc detachment for all arcs. For STEVE, the ASY-H index showed an abrupt enhancement ˜30 mins before the detachment, exhibiting a prominent bay-like structure. The ASY-H index shows an enhancement of 20 nT for STEVE and 5 nT for red and red+green arc. The detachment of arcs occurred immediately after the peak in ASY-H index for all arcs. The maximum magnitude of ASY-H index was ˜45 nT for STEVE, 25 nT for red and red+green arc. Thus, bay-like enhancement in the ASY-H index is significantly prominent for STEVE as compared to red and red+green arc. Although the magnitude of ASY-H index for red arc and red+green is same, the bay-like feature of ASY-H appeared prominently for red arc in comparison to red+green arc. The prominent bay-like ASY-H increase for STEVE probably indicates the connection of asymmetric ring current to the generation of STEVE during the substorm expansion phase.

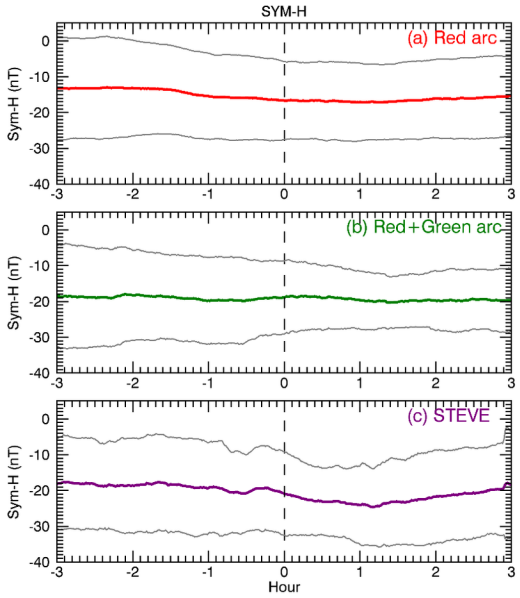

Figure 8: Same as Figure 5 but for SYM-H index.

3.2.6 X-component magnetogram at Boulder

In order to examine the local substorm activity, we also performed the similar analysis for H-component magnetogram at Boulder (BOU), shown in Figure 10. Although there is around 1-hr time difference from Boulder and Athabasca, the magnetic field variation at Boulder might provide an estimate of the middle latitude variation of X-component magnetogram at the longitude zone of Athabasca. Similar to the ASY-H index, the X-component magnetogram at Boulder began to increase gradually 1-hr prior to the arc detachment for all arcs; however, an abrupt increase ˜30-mins prior to the detachment is observed only for STEVE. The X-component magnetogram exhibits an enhancement of ˜20 nT for STEVE. By contrast, the enhancement of X-component magnetogram was gradual, broad, and weak (˜10 nT) for red arc and very weak for red+green arc (˜3 nT). Thus, the mid-latitude positive bay occurred prominently for STEVE as compared to red and red+green arc. The detachment of all arcs occurred immediately after the appearance of positive bay structure.

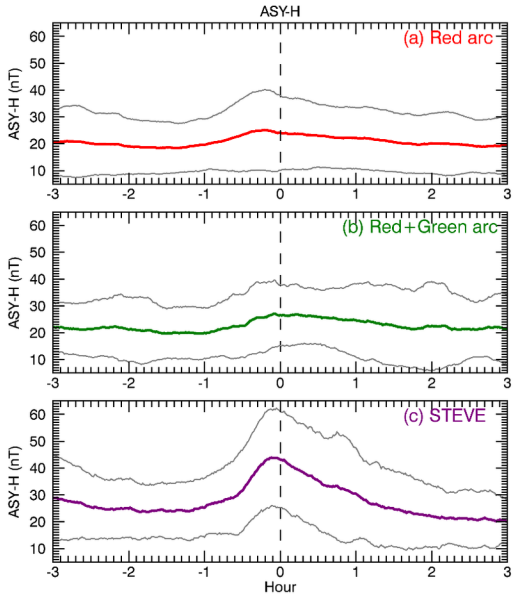

Figure 9: Same as Figure 5 but for ASY-H index.

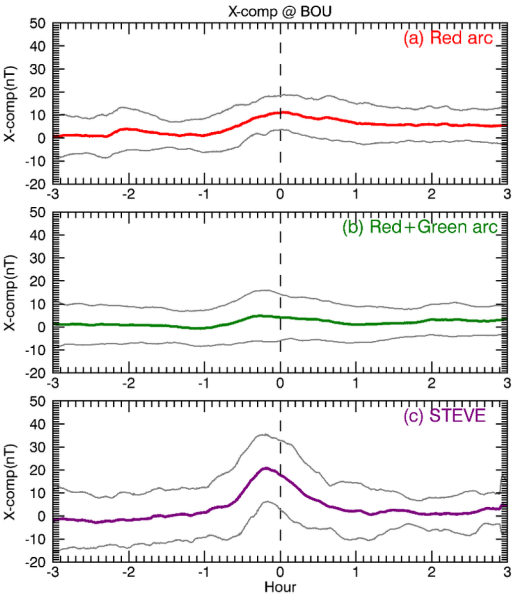

Figure 10: Same as Figure 5 but for X-component magnetogram at Boulder (BOU).

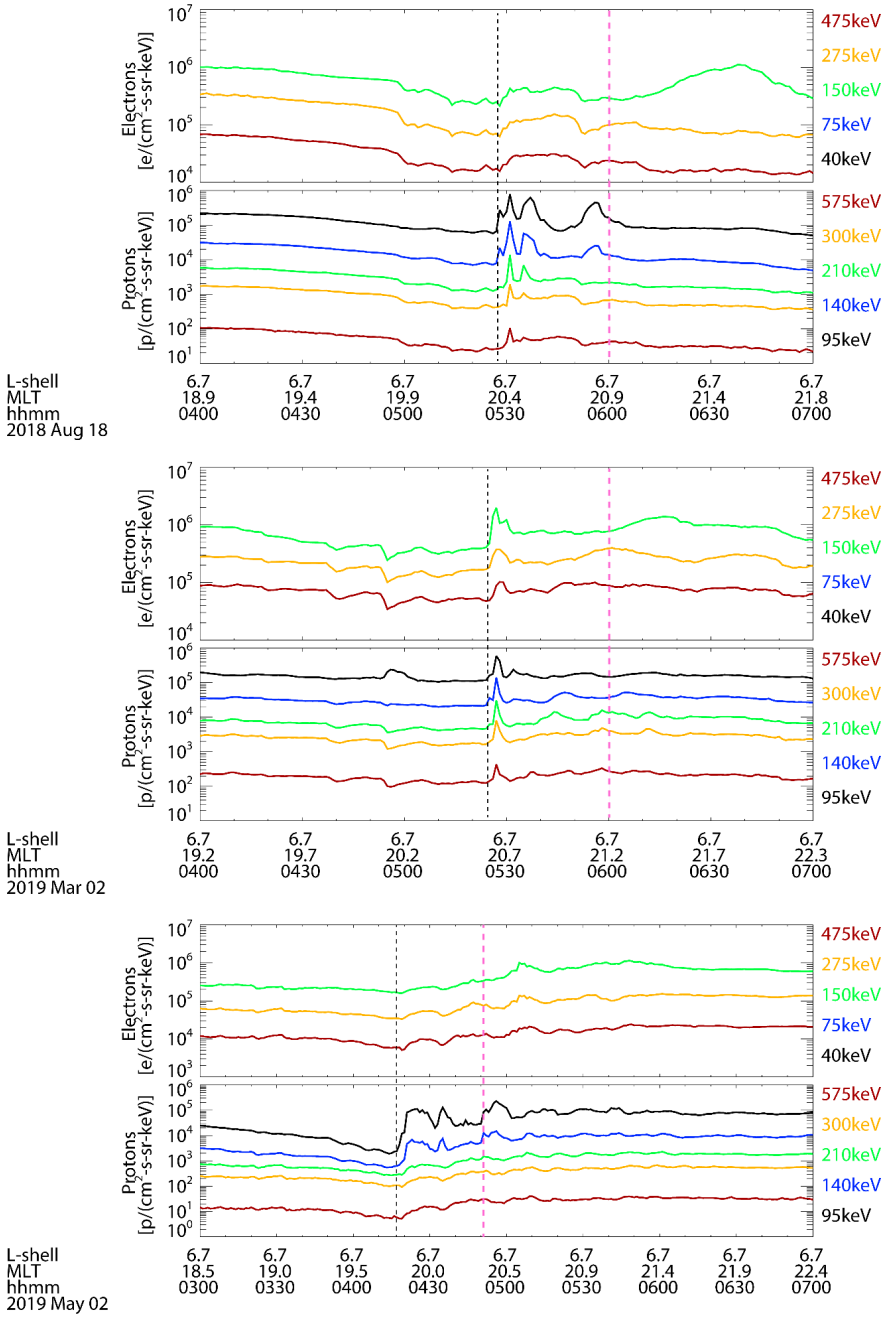

Figure 11: Examples of energetic electron and proton flux as a function of L-value, MLT, and UT for three STEVE events obtained from GOES-15 spacecraft. The interval of dispersionless enhancement is highlighted by black dashed lines. The purple dashed line represent the approximate time of STEVE detachment observed in the all-sky images.

3.3 Linkage of STEVE with substorm activity

We analyzed the GOES spacecraft magnetic field and particle flux data to identify the substorm associated injection at the geostationary orbit for STEVE events. Interestingly, we found that most of the STEVE events (20 events) were accompanied by the substorm associated injection at the geostationary orbit approximately

30 mins prior to the detachment of STEVE. Although we have used different GOES spacecrafts to identify the feature of diapolarization and substorm associated injection for all 26 STEVE events spanning from 2006 to 2019, here we have shown only three examples using GOES-15 particle flux (both electron and proton) data. Figure 11 shows three examples of energetic electron and proton fluxes from GOES-15 spacecraft as a function of L-value, MLT, and UT for STEVE events of (A) 18 August 2018, (B) 02 March 2019, and (C) 02 May 2019. GOES-15 was in the premidnight sector at 2000 MLT for these three events. The longitudinal difference of GOES-15 and Athabasca ASI is ˜63 degree. The detachment time of STEVE arc is highlighted by purple dashed line, as observed in the red-line ASI images at Athabasca. The black dotted lines indicate the start of dispersionless enhancement for both electron and proton fluxes. The dispersionless enhancement with a simultaneous increase of the electron (by a factor of ˜1.5-3.0) and ion fluxes (by a factor of ˜2 to an order of magnitude) at ˜0527-0552 UT was observed on 18 August 2018 (A) and STEVE started at 0600 UT. Similarly, at 0525-0532 UT, dispersionless enhancement by a factor of ˜4 was observed for 02 March 2019 (B) and STEVE observed at 0600 UT. For the event of 02 May 2019, STEVE began at 0450 UT and the dispersionless enhancement by a factor of ˜2-4 was observed at ˜0415-0435 UT. The enhancement of proton flux was found to be around one order of magnitude higher for lower energies (95 and 140 keV) for 02 May 2019 (C). Since GOES-15 observes near simultaneous dispersionless injections for both protons and electrons, the location of the injections must be close to the location of GOES-15 at 2000 MLT. GOES particle flux data confirm substorm onset before the STEVE events. Although not shown here, the events of diapolarization and substorm associated injection were also observed for red and red+green arcs.

4 Discussion

Based on 15-years of ASI data at Athabasca, we present a detailed comparative study on the occurrence characteristics of arc detachment from the main auroral oval for three different types of subauroral arc: pure red arc, red+green emission arc, and STEVE. Using monochromatic images at six different wavelengths, we identified 139 red arcs, 42 red+green arcs, and 26 STEVE events. The pure reds arcs observed in this study may be closely related to traditional SAR arcs (Takagi et al., 2018). However, we are not referring pure red arcs as SAR arc because of the association of red arcs with subauroral ionospheric drift (SAID) (Sazykin et al., 2002) and particle precipitation from the plasma sheet particularly in the midnight sector (Yadav et al., 2021b; under communication).

Covering two solar minimum periods, our results revealed that the detachment rate of red arcs was maximum during solar minimum and higher geomagnetic activity conditions. The geomagnetic activity (both solar wind and Ap index) were higher in 2019-2020 as compared to 2008-2009. Likewise, detachment rate of red arcs was higher in 2019-2020 as compared to 2008-2009. In comparison to red+green arcs, the detachment rate of red arcs was higher even for the lowest Ap years (2009-2010). The detachment rate of STEVE also maximized in solar minimum and high-geomagnetic activity year (2019). The red+green arc showed no occurrence or had minimum occurrence during low Ap and low solar wind speed years (2009-2011 and 2020). The detachment rate of both red and red+green arcs was low during the years of highest geomagnetic activity (2016-2017). Takagi et al. (2018) reported that the occurrence rate of SAR arc detachment was low in the solar maximum and minimum and high during the period of increase or decrease of solar activity. Alexeyev et al. (2009) also showed that the occurrence rate of SAR arcs has a maximum in the declining phase of solar activity. These studies also reported that the occurrence rate of SAR arcs correlated well with the geomagnetic activities represented by the Ap index. Note that both of these studies were based on nearly one-solar cycle data, whereas, 15-years of data used in the present study provides us a distinct opportunity to compare two solar minimum periods. Our results indicate that the detachment rate of red and red+green arc has dependence not only on geomagnetic activity but also on the solar flux.

It is well-known that the boundary of auroral oval expands with increasing geomagnetic activity, that is, the auroral zone expands equatorward at times of enhanced geomagnetic period. Thus, during high geomagnetic activity period, observed in 2016-2017, there is a high possibility that the auroral oval expands to reach latitudes of Athabasca. The magnetic latitudes of SAID is also known to shift equatorward with increasing geomagnetic activities (Karlsson et al., 1998; He et al., 2014). This implies that the probability of appearance

of subauroral arc should be reduced at the latitudes of Athabasca during higher geomagnetic activity, but at the same time, should have higher occurrence at lower latitudes. Mendillo et al. (2016) by analyzing 27-years of ASI data at Millstone Hill [42.6°N, 288.5°E, 56° invariant latitude] reported that occurrence of SAR arcs was minimum during solar minimum years and maximum during solar maximum years, opposite to what we observe at Athabasca.

We presented the magnetic local time (MLT) distribution of red, red+green arcs, and STEVE. STEVE is found to occur predominantly in the premidnight sector (highest occurrence at 22-24 MLT, and then at 20-22 MLT). Using THEMIS ASI and REGO database Gallardo-Lacourt et al. (2018) identified 28 STEVE events between 22 and 01 MLT. A large majority of SAID occurred in the premidnight sector (2000-2300 MLT) with strength being higher for events close to 2200 MLT (Karlsson et al., 1998; Figueiredo et al., 2004). Being an optical manifestation of SAID (MacDonald et al., 2018; Archer et al., 2019), STEVE showed good correlation with the occurrence characteristics of SAID. Red and red+green arcs exhibit maximum detachment rate around the midnight sector (highest occurrence at 00-02 MLT, and then at 22-24 MLT). Using Athabasca ASI (2006-2016), Takagi et al. (2018) reported that the occurrence rate of SAR arc detachment was highest in the premidnight sector (20–22 MLT). They suggested that the detachment of SAR arcs may correspond to the dynamical injection of ring current ion populations into the inner magnetosphere. Note that the study of Takagi et al. (2018) is different from the present study because they considered the total occurrence rate (from the time of detachment till until the arc remained detectable in the ASI images) of SAR arcs, whereas we have focused solely on the detachment rate. In addition, Takagi et al. (2018) perceived STEVE events as the SAR arc. In the present study, highest detachment rate of red and red+green arcs is observed around the midnight sector, suggesting that the low-energy particle (<10 keV) precipitation from plasma sheet might also play a role in the formation of subauroral arcs around the midnight sector (Yadav et al., 2021b; under communication).

In section 3.2, we performed superposed epoch analysis to compare various geomagnetic activity indices during the detachment of red, red+green arcs, and STEVE. Results reveal that STEVE occurred during higher geomagnetic activity as compared to that observed for red and red+green arcs. Gallardo-Lacourt et al. (2018) reported that STEVE occurred at the end of a prolonged substorm expansion phase (˜60 min). However, our results show that the substorm expansion phase persisted for ˜60 mins (both in AL index and X-component magnetogram) not only for STEVE but also for red and red+green arcs. The notable point is that substorm intensities estimated by the magnetic field variations were ˜2-3 times higher for STEVE as compared to red and red+green arcs.

In general, all arcs occurred towards the end of expansion phase and beginning of recovery phase, as already shown in the earlier studies for STEVE (Gallardo-Lacourt et al. 2018) and SAR arcs (Takagi et al., 2018). The X-component magnetogram at Fort Smith indicated that the detachment of STEVE coincided with the sharp recovery from the expansion phase and the beginning of additional activity in the recovery phase of a substorm. Based on three STEVE events, Yadav et al. (2021a) first highlighted the association of STEVE detachment and brightness with the additional activities in the recovery phase of a substorm. Our results, based on 26 STEVE events, provide further credence to the findings of Yadav et al. (2021a) that triggering of STEVE requires additional energization, observed in terms of additional activities in the recovery phase of a substorm. Gallardo-Lacourt et al. (2018) identified streamers within the auroral oval for STEVE events, indicating the association of STEVE with substorm activity.

Our results, for the first time, show the association of STEVE with ASY-H index in terms of a prominent bay-like enhancement just prior to the detachment of STEVE. The detachment of STEVE occurred immediately after the peak in ASY-H index. A sharp bay-like enhancement is also observed for X-component magnetogram at Boulder, a mid-latitude station in the longitude zone of Athabasca. The ASY-H index is associated with an intensification of asymmetric ring current in the dusk sector (Nishida, 1978). The bay-like variations of H- and D-components might indicate the onset of substorm expansion (Rostoker et al., 1980). Although the bay-like enhancement is also observed for the red and red+green arcs, it was weak (5 nT) and broad compared to STEVE (20 nT). The association of SAR arc with a bay-like structure in the ASY-H index

is shown in the past studies (e.g., Ievenko et al., 2008). Unlike red arcs, a clear bay-like structure prior to the detachment of arc is not observed for green+red arc, indicating that the mechanism for the formation of red+green arc may be different from the red arc. It is notable that positive bay enhancement in ASY-H index for STEVE was 4 times stronger than red and red+green arcs. This suggests the strong association of STEVE with the asymmetry in ring current.

Lastly, in order to further provide evidence to the association of STEVE with substorms, we analyzed GOES particle flux. Results unveil that majority (20/26) of the STEVE events were accompanied by the dispersionless injection of both electron and proton flux at geosynchronous orbit, a ubiquitous characteristic of substorms. Such enhancements were observed ˜30 mins prior to the detachment of STEVE into the nightside. Note that such particle injection events at the geostationary orbit were also observed often for red and red+green arcs. The dispersionless injection of both electron and proton flux at geosynchronous orbit for SAR arc was reported in the past (e.g., Ievenko et al., 2008). However, the peculiar features in the magnetic field was observed only for STEVE, for example, i) both ASY-H index and X-component magnetogram at Boulder showed an abrupt enhancement ˜30-mins prior to the STEVE arc detachment, forming a feature of prominent positive bay-like enhancement before the detachment of STEVE arc ii) the SYM-H index and X-component magnetogram at Athabasca showed small enhancement ˜30 mins prior to the detachment of STEVE, and iii) the X-component magnetogram at Fort Smith shows the presence of additional activities in the recovery phase of substorms. Such features were not observed for red arcs and red+green arcs. These results unambiguously indicate that STEVE develops after the substorm associated energy injection and consequent intensification of asymmetric ring current.

5 Conclusions

While individual statistics of SAR arc and STEVE have been reported in previous studies, here we present for the first time comparative statistical study of three types of subauroral arc from the same station—an aspect not yet addressed. We have used 15-years (2006-2020; covering two solar minimum) of ASI observation at Athabasca to perform a comparative statistical study of red arcs, red+green arcs, and STEVE. The most commonly observed arc was red arc (139 events), followed by red+green arc (42 events) and STEVE (26 events), an extremely rare phenomenon.

We found that the detachment rate of red arcs was high for the solar minimum and high geomagnetic activity years, displaying dependence on both solar flux and geomagnetic activity. The detachment rate of red+green arc was higher for moderate geomagnetic activity years and had minimal or no occurrence for low geomagnetic activity. The detachment rate of STEVE also maximized in solar minimum and high-geomagnetic activity year (2019). Given that auroral oval expands equatorward with increasing geomagnetic activity, the occurrence of all subauroral arcs was low during peak geomagnetic activity year (2016-2017), indicating that occurrence rate of arcs has a dependence on the location of observing station. The detachment rate of STEVE was higher in the premidnight sector, whereas red arcs and red+green arcs exhibit higher detachment rate around the midnight sector.

In order to provide insights on the specific geomagnetic conditions during STEVE, we performed a comparative superposed epoch analysis for various geomagnetic activity indices for red arcs, red+green arcs, and STEVE. Results reveal that STEVE occurred during relatively higher geomagnetic activity, the substorm activity was ˜2-3 times higher for STEVE as compared to other arcs. The ASY-H index shows the prominent bay-like enhancement with a peak just prior to the detachment of STEVE, the bay-like enhancement was ˜4 times higher for STEVE as compared to other arcs.

Majority of STEVE events were accompanied by the feature of dispersionless injection for both electron and proton flux at the geosynchronous orbit ˜30 mins prior to the STEVE detachment. The feature of dispersionless injection for particle flux at the geosynchronous orbit was also observed for red arcs and red+green arcs. However, the geomagnetic activity indices show peculiar features for STEVE and not for other arcs. For example, i) both ASY-H index and X-component magnetogram at Boulder showed the presence of prominent positive bay-like enhancement before the detachment of STEVE, ii) the SYM-H index

and X-component magnetogram at Athabasca showed small enhancement ˜30 mins prior to the STEVE detachment, and iii) the X-component magnetogram at Fort Smith and AL index showed the presence of additional activities during the time of STEVE detachment. The development of STEVE occurred at the end of substorm expansion phase and significant intensification of asymmetric ring current in the dusk sector.

Acknowledgement

- The all-sky imager data at Athabasca are available through ISEE/Nagoya University. Quick-look plots of the OMTI data are available at http://stdb2.isee.nagoya-u.ac.jp/omti/ and the data can be accessed from the ERG Science Center operated by ISAS/JAXA and ISEE/Nagoya University (https://ergsc.isee.nagoya-u.ac.jp/data/ergsc/ground/camera/omti/asi/).
- The all-sky imager at Athabasca was calibrated using optical facilities of National Institute of Polar Research, Japan (Ogawa et al., 2020). It is housed in facilities developed and supported by the Canada Foundation for Innovation.
- The solar wind data and geomagnetic activity indices (both one-minute and one-year resolution) were obtained from the SPDF, NASA, USA (http:// omniweb.gsfc.nasa.gov)
- The GOES spacecraft magnetic field and particle data from magnetic field (MAG), MAGnetospheric Electron Detector (MAGED) and MAGnetospheric Proton Detector (MAGPD) were provided by the NOAA National Geophysical Data Center (https://satdat.ngdc.noaa.gov/sem/goes/data/).
- Ground-based magnetic field data is the part of following networks. Athabasca (ATHA) data from this period was part of the AUTUMN network operated by Athabasca University. Fort Smith (FSMI) is part of CARISMA (Mann et al., 2008) network. We thank I.R. Mann, D.K. Milling and the rest of the CARISMA team for data. CARISMA is operated by the University of Alberta, funded by the Canadian Space Agency. Boulder (BOU) is a part of the US Geological Survey network. Original data provided by the USGS Geomagnetism Program (http://geomag.usgs.gov). All the magnetic field data are downloaded from the THEMIS website (http://themis.ssl.berkeley.edu/data/themis/thg/mirrors/mag/).
- We have used the Space Physics Environment Data Analysis Software (SPEDAS) tool (Angelopoulos et al., 2019) to download and analyze the 1-min geomagnetic activity indices, ground-based magnetic field, and GOES particle flux data.
- This work is supported by JSPS KAKENHI (16403007, 19403010, 20244080, 23403009, 25247080, 15H05815, and 16H06286).

References

Anger, C. D., Moshupi, M. C., Wallis, D. D., Murphree, J. S., Brace, L. H., & Shepherd, G. G. (1978). Detached auroral arcs in the trough region. *Journal of Geophysical Research* , 83(A6), 2683–2689. https://doi.org/10.1029/JA083iA06p02683

Angelopoulos, V. et al. (2019), The Space Physics Environment Data Analysis System (SPEDAS). *Space Science Review* , 215. https://doi.org/10.1007/s11214-018-0576-4.

Alexeyev, V., Ievenko, I., & Parnikov, S. (2009). Occurrence rate of SAR arcs during the 23rd solar activity cycle. *Advances in Space Research* , *44* , 524–527. https://doi.org/10.1016/j.asr.2009.04.024

Archer, W. E., Gallardo-Lacourt, B., Perry, G. W., St-Maurice, J.-P., Buchert, S. C., & Donovan, E. F. (2019). Steve: The optical signature of intense subauroral ion drifts. *Geophysical Research Letters* ,*46* , 6279–6286. https://doi.org/10.1029/2019GL082687

Barbier, D. (1958). The auroral activity at low latitudes. *Annals of Geophysics* , 1, 4334–4355.

Chu, X., Malaspina, D., Gallardo-Lacourt, B., Liang, J., Andersson, L., Ma, Q., et al (2019), Identifying STEVE's Magnetospheric Driver Using Conjugate Observations in the Magnetosphere and on the Ground.*Geophysical Research Letters,* 46. https://doi.org/10.1029/2019GL082789

Cornwall, J. M., Coroniti, F. V., & Thorne, R. M. (1971), Unified theory of SAR arc formation at the plasmapause. *Journal of Geophysical Research* , 76, 4428–4445. https://doi.org/10.1029/JA076i019p04428

Cole, K. (1965), Stable auroral red arcs, sinks for energy of Dst main phase. *Journal of Geophysical Research* , 70, 1689–1706, doi:10.1029/JZ070i007p01689.

Figueiredo, S., T. Karlsson, and G. T. Marklund (2004), Investigation of subauroral ion drifts and related field-aligned currents and ionospheric Pedersen conductivity distribution, *Annales Geophysicae* , 22, 923–934

Frey, H. U. (2007). Localized aurora beyond the auroral oval.*Reviews of Geophysics,* 45(1), 1003. https://doi.org/10.1029/2005RG000174

Gallardo-Lacourt, B., Nishimura, Y., Donovan, E., Gillies, D. M., Perry, G. W., Archer, W. E., et al. (2018). A statistical analysis of STEVE.*Journal of Geophysical Research: Space Physics,* 123, 9893–9905. https://doi.org/10.1029/2018JA025368

Gallardo-Lacourt, B., Frey, H.U. & Martinis, C. (2021). Proton Aurora and Optical Emissions in the Subauroral Region. *Space Science Reviews,* 217, 10. https://doi.org/10.1007/s11214-020-00776-6

Galperin, Y., Ponomarev, V. N., and Zosimova, A. G. (1974). Plasma convection in the polar ionosphere, *Annales Geophysicae* , 30, 1.

Gillies, D. M., Donovan, E., Hampton, D., Liang, J., Connors, M., Nishimura, Y., et al. (2019). First observations from the TREx Spectrograph: The optical spectrum of STEVE and the Picket Fence phenomena. *Geophysical Research Letters* , 46, 7207–7213. https://doi.org/10.1029/2019GL083272

Hoch, R. J., Stable auroral red arcs, *Reviews of Geophysics* , 11, 935, 1973.

He, F., X.-X. Zhang, and B. Chen (2014), Solar cycle, seasonal, and diurnal variations of subauroral ion drifts: Statistical results,*Journal of Geophysical Research: Space Physics* , 119, 5076–5086, doi:10.1002/2014JA01980

Inaba, Y., Shiokawa, K., Oyama, S., Otsuka, Y., Connors, M., Schofield, I., et. al. (2021). Multi-event analysis of plasma and field variations in source of stable auroral red (SAR) arcs in inner magnetosphere during non-storm-time substorms. *Journal of Geophysical Research: Space Physics* , 126, e2020JA029081. https://doi.org/10.1029/2020JA029081

Ievenko, I.B., Parnikov, S.G., Alexeyev, V.N. (2008). Relationship of the diffuse aurora and SAR arc dynamics to substorms and storms,*Advances in Space Research* , 41, 8, 1252-1260

Karlsson, T., G. T. Marklund, and L. G. Blomberg (1998), Subauroral electric fields observed by the Freja satellite: A statistical study,*Journal of Geophysical Research* , 103(A3), 4327–4314, doi:10.1029/97JA00333.

Kozyra, J. U., E.G. Shelly, R. H. Comfort, L. H. Brace, T. E. Cravens, and A. F. Nagy, The role of ring current O + in the formation of stable red arcs, *Journal of Geophysical Research* , 92, 7487, 1987.

Kozyra, J. U., & Nagy, A. F. (1997), High-altitude energy source(s) for stable auroral red arcs. *Reviews of Geophysics* , 35, 155-190, 96RG03194.

MacDonald, E. A., Donovan, E., Nishimura, Y., Case, N. A., Gillies, D. M., Gallardo-lacourt, B., et al. (2018). New science in plain sight: Citizen scientists lead to the discovery of optical structure in the upper atmosphere. *Science Advances* , 4(March), 16–21. https://doi.org/10.1126/sciadv.aaq0030

Mann, I. R., et al. (2008). The upgraded CARISMA magnetometer array in the THEMIS era, *Space Science Review* , 141, 413–451, doi:10.1007/s11214-008-9457-6.

Moshupi, M. C., Anger, C. D., Murphree, J. S., Wallis, D. D., Whitteker, J. H., Brace L. H. (1979), Characteristics of trough region auroral patches and detached arcs observed by Isis 2. *Journal of Geophysical Research: Space Physics* , 84 (A4), 1333-1346. https://doi.org/10.1029/JA084iA04p01333

Mendillo, M., Baumgardner, J., & Wroten, J. (2016). SAR arcs we have seen: Evidence for variability in stable auroral red arcs. *Journal of Geophysical Research: Space Physics* , 121(1), 245–262. https://doi.org/10.1002/2015JA021722

Nagy, A. F., Roble, R. G., & Hays, P. B. (1970). Stable mid-latitude red arcs: Observations and theory. *Space Science Reviews* , 11, 709–727. https://doi.org/10.1007/BF00177029

Nishida, A. (1978). Geomagnetic Diagnosis of the Magnetosphere.*Springer, New York* .

Sazykin, S., Fejer, B. G., Galperin, Y. I., Zinin, L. V., Grigoriev, S. A., & Mendillo, M. (2002). Polarization jet events and excitation of weak sar arcs. *Geophysical Research Letters,* 29(12), 26-1–26-4. https://doi.org/10.1029/2001GL014388

Ogawa, Y., Kadokura, A., Ejiri, M. K. (2020), Optical calibration system of NIPR for aurora and airglow observations. *Polar Science* , Volume 26. https://doi.org/10.1016/j.polar.2020.100570

Ozaki, M., Shiokawa, K., Horne, R. B., Engebretson, M. J., Lessard, M., Ogawa, Y., et al. (2021). Magnetic conjugacy of Pc1 waves and isolated proton precipitation at subauroral latitudes: Importance of ionosphere as intensity modulation region. *Geophysical Research Letters,* 48, e2020GL091384. https://doi.org/10.1029/2020GL091384

Rees, M. H., and Roble, R. G. (1975). Observations and theory of the formation of stable auroral red arcs, *Reviews of Geophysics* , 13, 201.

Rostoker, G. Akasofu, S.I. Foster, J. et al. (1980). Magnetospheric substorm – Definition and signatures. *Journal of Geophysical Research* , (A4), 1663-1668

Smiddy, M., Kelley, M. C., Burke, W., Rich, F., Sagalyn, R., Shuman, B., Hays, R., and Lai, S. (1977). Intense poleward-directed electric fields near the ionospheric projection of the plasmapause, *Geophysical Research Letters,* 4, 543 –546.

Spiro, R. W., Heelis, R. A., and Hanson, W. B. (1979). Rapid subauroral ion drifts observed by Atmospheric Explorer C, *Geophysical Research Letters,* 6, 657 – 660.

Shiokawa, K., Katoh, Y., Satoh, M., Ejiri, M. K., Ogawa, T., Nakamura, T., Tsuda, T., & Wiens, R. H. (1999). Development of optical mesosphere thermosphere imagers (OMTI). *Earth, Planets and Space,* 51, 887–896. https://doi.org/10.1186/BF03353247

Shiokawa, K., Hosokawa, K., Sakaguchi, K., Ieda, A., Otsuka, Y., Ogawa, T., & Connors, M. (2009). The optical mesosphere thermosphere imagers (omtis) for network measurements of aurora and airglow. *AIP Conference Proceedings,* 1144(1), 212–215. https://doi.org/

10.1063/1.3169292

Shiokawa, K., Katoh, Y., Hamaguchi, Y., Yamamoto, Y., Adachi, T., Ozaki, M., et al. (2017). Ground-based instruments of the pwing project to investigate dynamics of the inner magnetosphere at subauroral latitudes as a part of the erg-ground coordinated observation network. *Earth Planets and Space,* 69(1), 160. https://doi.org/10.1186/s40623-017-0745-9

Sakaguchi, K., Shiokawa, K., Miyoshi, Y., Otsuka, Y., Ogawa, T., Asamura, K., & Connors, M. (2008). Simultaneous appearance of isolated auroral arcs and Pc 1 geomagnetic pulsations at subauroral latitudes.*Journal of Geophysical Research* , 113(A5), A05201. https://doi.org/10.1029/2007ja012888

Takagi, Y., Shiokawa, K., Otsuka, Y., Connors, M., & Schofield, I. (2018). Statistical analysis of SAR arc detachment from the main oval based on 11-year, all-sky imaging observation at Athabasca, Canada.*Geophysical Research Letters* , 45, 11,539–11,546. https://doi.org/10.1029/2018GL079615

Yadav, S., Shiokawa, K., Otsuka, Y., Connors, M., and St. Maurice, J.-P. (2021a), Multi-wavelength imaging observations of STEVE at Athabasca, Canada. *Journal of Geophysical Research: Space Physics* , 125, https://doi.org/10.1029/2020JA028622.

Yadav, S., Shiokawa, K., Oyama, S., Inaba, Y., Takahashi, N., Seki, K., et al. (2021b), Study of an equatorward detachment of auroral arc from the oval using ground-space observations and the BATS-R-US

– CIMI model. Under second review in *Journal of Geophysical Research: Space Physics* .

Zhou, S., Luan, X., Burch, J. L., Yao, Z., Han, D. S., Tian, C., et. al. (2021), A possible mechanism on the detachment between a subauroral proton arc and the auroral oval. *Journal of Geophysical Research: Space Physics,* 126, e2020JA028493. https://doi.org/10.1029/2020JA028493

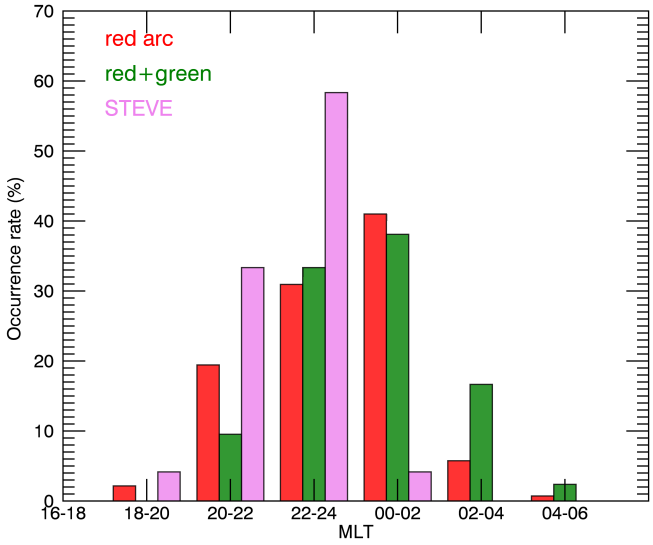

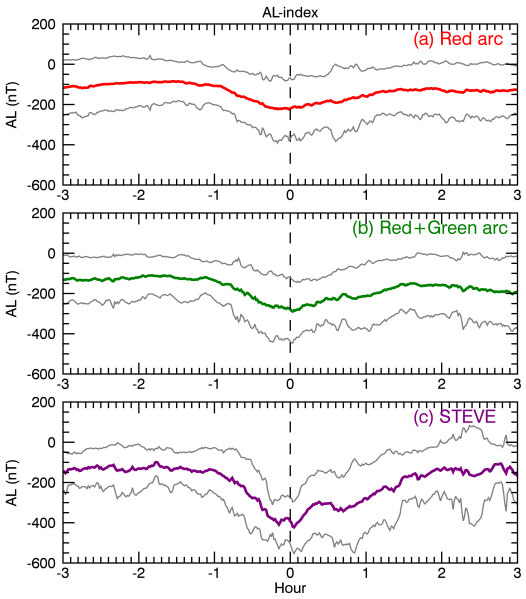

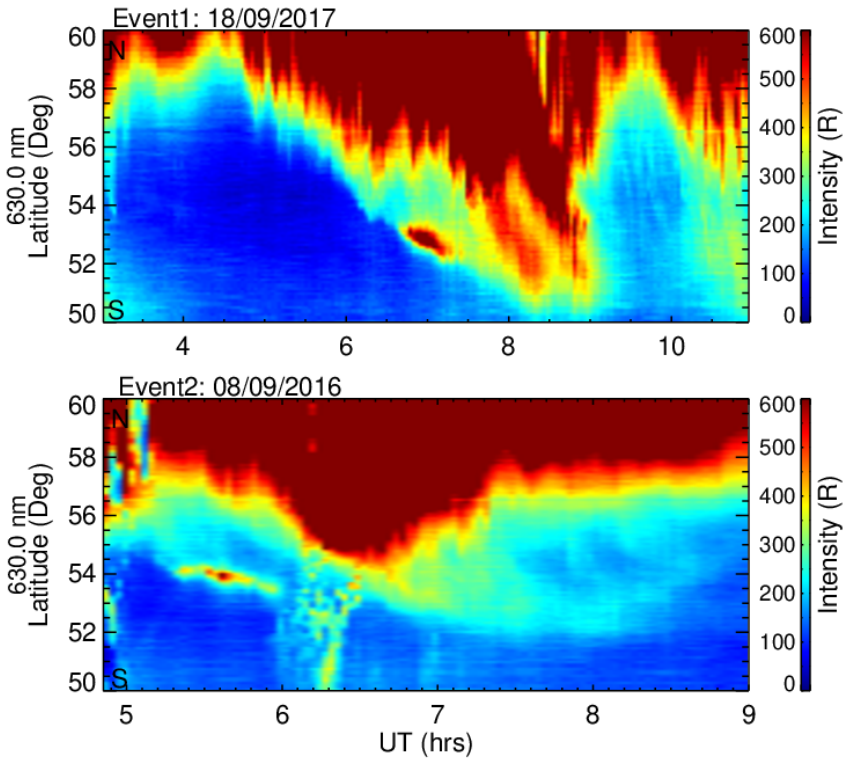

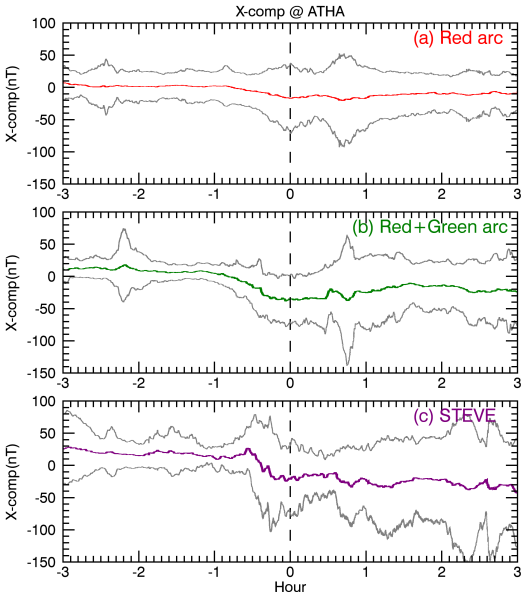

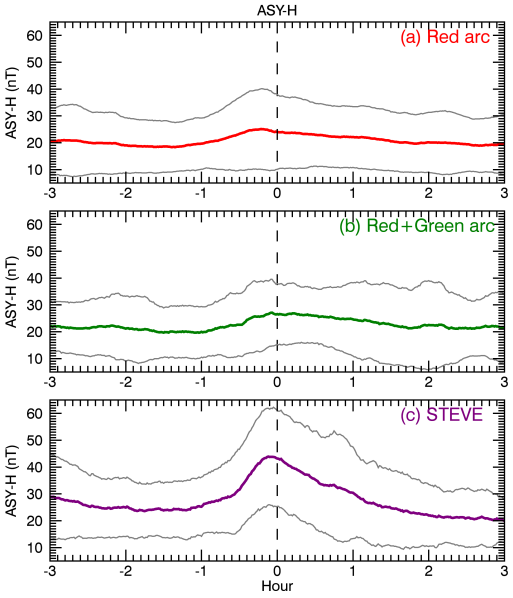

Statistical study of subauroral arc detachment at Athabasca, Canada: new insights on STEVE

Sneha Yadav[1], Kazuo Shiokawa[1], Yuichi Otsuka[1], Martin Connors[2,3]

[1]Institute for Space-Earth Environmental Research, Nagoya University, Nagoya, Japan

[2]Athabasca University Observatories, Athabasca University, Athabasca, Alberta, Canada

[3]Department of Physics and Astronomy, University of Calgary, Calgary, Alberta, Canada

Corresponding author: Sneha Yadav (sneha.yadav84@gmail.com)

Key Points:

- The first comparative statistical study of arc detachment from the main auroral oval at the subauroral latitudes for three types of arcs.
- The substorm intensities estimated by the magnetic field variations were ~2-3 times higher for STEVE as compared to other arcs.
- The ASY-H index shows prominent bay-like structure (~4 times higher as compared to other arcs) just prior to the STEVE detachment.

Abstract

We present the first comparative statistical study of subauroral arc detachment from the main auroral oval at Athabasca (magnetic latitude = 61.5°N), Canada, for three different types of subauroral arcs: pure red arc, red arc with simultaneous emission in green-line (red+green arc), and STEVE (strong thermal emission velocity enhancement). Based on 15-years (2006-2020) of all-sky imaging observations, this study not only uncovers the occurrence characteristics of different arcs but also provides important insights into the specific geomagnetic conditions under which STEVE develops. Red arc was the most common subauroral arc (139 events), followed by red+green arc (42 events), and STEVE (26 events) was a rare phenomenon. The detachment rate of red and red+green arcs exhibits dependence on both the solar flux and geomagnetic activity. The detachment rate of STEVE was higher during premidnight, whereas red and red+green arcs were higher around the midnight sector. The geomagnetic activity was relatively higher for STEVE, the decrease in the AL index and local X-component magnetic variations were ~2-3 times higher for STEVE as compared to other arcs. STEVE shows a strong association with asymmetric ring current in terms of prominent bay-like enhancement in ASY-H index prior to the STEVE detachment. Such bay-like enhancement was ~4 times higher for STEVE as compared to other arcs. STEVE events were accompanied by dispersionless injection for both electron and proton flux at the geosynchronous orbit. These results unambiguously suggest that STEVE develops after the substorm associated energy injection and significant intensification of asymmetric

ring current.

1 Introduction

The subauroral ionosphere is the region where magnetic field changes from stretched to more dipolar field like topology. The nightside poleward part of the subauroral ionosphere is affected by electron precipitation from the plasma sheet, whereas the equatorward part is maintained by plasma from the plasmasphere. The ring current is the energy source for the magnetospheric electron heat flux in the subauroral region (e.g. Hoch, 1973; Rees and Roble, 1975; Kozyra et al., 1987). During geomagnetically disturbed intervals, the heated electrons, generated by the interaction between plasmasphere and ring current, fall into the ionosphere at subauroral latitudes along magnetic field lines. Further, the strong poleward electric field located equatorward of the auroral oval produces latitudinally narrow regions of duskward plasma flow at subauroral latitudes known as polarization jet (Galperin et al., 1974) or SAID (subauroral ion drifts) (Smiddy et al., 1977; Spiro et al., 1979). Thus, the subauroral ionosphere experiences a number of highly dynamic processes related to convection electric field, coupling of trapped energetic particles, and thermal plasma, causing the formation of various types of optical features in this region (e.g., Frey, 2007, for a review). One of the most fascinating optical features observed at the subauroral ionosphere is the 'subauroral arc'. Unlike typical auroral arcs, the subauroral arcs may not be always caused by direct excitation from energetic particle precipitation (e.g., Gallardo-Lacourt et al. 2021, for a review).

Stable auroral red (SAR) arcs are most common type of subauroral arc and have been studied extensively since their discovery in the 1950s (Barbier, 1958). The red-line emissions of SAR arcs are caused by the interaction of the inner edge of the ring current with the contracted plasmasphere. The Coulomb collision is considered as a main mechanism through which energy is transferred from ring current ions (several tens of keV) to plasmaspheric electrons (energies less than 1 eV) (Cole, 1965; Kozyra et al., 1987). Energized thermal electrons can transport energy down to the ionosphere via heat conduction or as a low-energy electron flux (e.g., Cole, 1965), exciting atomic oxygen to the $O(^1D)$ state. SAR arcs with weak green-line (557.7 nm) emission have been reported by past studies (e.g., Mendillo et al., 2016; Inaba et al., 2021). A newly recognized subauroral optical structure, known as STEVE (strong thermal emission velocity enhancement), has also grasped the attention of the space physics community in recent years (e.g., MacDonald et al., 2018). STEVE is a visible purple color arc, often occasionally accompanied by green ray structure at the lower altitudes, known as picket fence.

Similar to SAR arc, STEVE is shown to be associated with enhancement in temperature and westward ion drift (MacDonald et al., 2018). Both SAR arcs and STEVE have been reported to occur in the recovery phase of substorms (Takagi et al., 2018; Gallardo-Lacourt et al., 2018). They are generated at or just inside the plasmapause (Cornwall et al., 1971; Kozyra et al., 1997; Chu et al., 2019). Although STEVE shows some similarities to SAR arcs in terms of

their location and occurrence, the two phenomena differ markedly from each other. While SAR arcs are subvisual, spectrally pure red-line emission with little or no green emission, and long-lived (10 hours or longer) (e.g. Nagy et al., 1970), purple STEVE is visible to the naked eye, latitudinally narrow, and short-lived (~around one-hour) (Gallardo-Lacourt et al., 2018). Unlike that of monochromatic SAR arcs (only 630.0 nm), STEVE spectrum consists of a continuum spectrum spanning between ~400 and 730 nm (Gillies et al., 2019).

Recent studies have shown that common feature of both SAR arcs and STEVE is equatorward arc detachment from the main auroral oval (e.g., Shiokawa et al., 1999; 2009; 2017; Takagi et al., 2018; Gallardo-Lacourt et al., 2018; Yadav et al. 2021a). Using an all-sky imager (ASI) at Athabasca, Takagi et al. (2018) and Yadav et al. (2021) reported that, initially, SAR arcs and STEVE arcs appeared very close to the main auroral oval. As time progressed, this arc separated itself from the oval and moved equatorward when the main oval returned to higher latitudes. This feature is referred as the "detachment of arc from the oval". Anger et al. (1978) and Moshupi et al. (1979) first used the term "detached arcs" to describe the arc-like auroral features equatorward of the auroral oval observed by the ISIS 2 satellite scanning photometer. The ISIS-2 detached arcs displayed emissions in 391.4 nm (N_2^+) and 557.7 nm with no emission enhancement in 630.0 nm and occurred in the afternoon sector, hence are referred as "afternoon detached arcs". The detached arcs in the midnight sector at the subauroral latitudes with emission in both red- and green line (red+green arc) have been shown to be associated with the low-energy particle precipitation from the plasma sheet (Yadav et al., 2021b; under communication). Detached proton arcs have also been observed in the subauroral region (Sakaguchi et al., 2008; Ozaki et al., 2021; Zhou et al., 2021; and reference therein). The proton arcs have been shown to be formed by the precipitation of high-energy ions caused by the interactions of electromagnetic ion cyclotron (EMIC) waves with ring current ions (e.g., Sakaguchi et al., 2008). On account of the generation mechanism of subauroral proton arcs, we have not considered protons arcs in the present study.

In the past, individual statistical study of SAR arc and STEVE have been carried out. For example, Gallardo-Lacourt et al. (2018) performed a statistical analysis for 28 STEVE events using Time History of Events and Macroscale Interactions during Substorms (THEMIS) all-sky imager and the Redline Emission Geospace Observatory (REGO) database that is, they performed the statistical analysis of STEVE using multiple sites. Based on 11 years of ASI observations at Athabasca, Takagi et al. (2018) performed a statistical analysis of detached SAR arc. Note that in the study of Takagi et al. (2018), weak 557.7-nm emission also accompanied the SAR arc for some cases. A statistical study of subauroral arc with simultaneous emission in red and green-line, hereafter referred as red+green arc, remains unexplored. A detailed comparative statistical study of geomagnetic conditions for different subauroral arcs at a single station is also missing from the literature. Here, we present a comparative statistical analysis on the detachment of red arcs, red+green arcs, and STEVE with reference to

solar flux, geomagnetic activity, and magnetic local time (MLT) distribution. Such a comparative study will not only enable disentangling the mysteries associated with STEVE, but also shed light on the specific geomagnetic conditions under which the arcs detached as red arc, red+green arc, and STEVE.

2 Database and methodology

One of the requirement to perform the statistical analysis is long-term availability of all-sky imaging observations for the arc detection. An OMTI (Optical Mesosphere Thermosphere Imager) (Shiokawa et al., 1999, 2009) all-sky imager (ASI) (camera no. 7) has been operating at Athabasca (54.6°N, 246.3°E, magnetic latitude: 61.5°N, L = 4.4), Canada, since September 3, 2005. Magnetic midnight for this ASI occurs at ~8.1 UT. In the present study, we have used 15-years of continuous ASI observations from 2006-2020. The camera has a 180° field-of-view fish-eye lens, seven band-pass optical filters, and a thermoelectrically cooled CCD with 512 × 512 pixels. In order to increase the signal to noise ratio, CCD images are processed with 2 × 2 binning, so that the images had a resolution of 256 × 256 pixels. The seven band-pass filters of this camera allow measurement of airglow/auroral emissions at specific wavelengths: OI at 557.7 nm, OI at 630.0 nm, H at 486.1 nm, Na at 589.3 nm, OH bands at 720–910 nm, OI at 844.6 nm, and nominal background at 572.5 nm. In this study, we have used images at all the wavelengths except for OH bands. The details about the exposure times of the images at different wavelengths are given in Yadav et al. (2021a).

The raw images are projected into the geographical latitude/longitude coordinates by assuming that the emission intensity has a peak at 250 km altitude for 630.0 nm and 120 km for the other wavelengths. We have constructed North-South (NS) keograms by stripping the slices of airglow images at the longitude of Athabasca (246.3°E). The keograms facilitate the study of temporal variations in the auroral emission intensities and their latitudinal motion.

As mentioned earlier, proton arcs are not considered in this study. Subauroral proton arcs, which exhibit emission in 557.7 nm, 630.0 nm, and 486.1 nm (H), have been shown to occur simultaneously with Pc 1 geomagnetic pulsations in the frequency range of the EMIC wave (e.g., Sakaguchi et al., 2008). An induction magnetometer has been operating at Athabasca since September 2005. The induction magnetometer measures variation of a three-component geomagnetic field with a sensitivity of 0.45 (V/nT) at 6 Hz with a turnover frequency of 6 Hz. The dynamic magnetic field spectra used to decipher the presence of Pc 1 geomagnetic pulsations is available at the ISEE magnetometer website (https://stdb2.isee.nagoya-u.ac.jp/magne/induction/index.html). Detached red+green arcs with simultaneous occurrence of Pc 1 geomagnetic pulsation were eliminated from the present study.

To study the solar flux and geomagnetic activity dependence of detached arcs, we obtained the yearly solar flux and geomagnetic indices from the NASA's Space Physics Data Facility (SPDF) OMNI database. The 1-min resolution ge-

omagnetic indices were also obtained from the OMNI database, used to examine the geomagnetic conditions during the detachment of arcs. The magnetometer data at Athabasca (ATHA), Fort Smith (FSMI; Lat 60.0°N, Long 248.2°N; magnetic latitude: 67.28°N), and Boulder (BOU; Lat 40.1°N, Long 254.7; magnetic latitude: 48.7°N) were used to access the substorm activity in the longitude zone of Athabasca ASI. Fort Smith is located in the auroral oval, whereas Boulder is a middle latitude station.

The magnetic field (MAG) and particle data from MAGnetospheric Electron Detector (MAGED) and MAGnetospheric Proton Detector (MAGPD) onboard Geostationary Operational Environmental Satellite (GOES) were used to identify the substorm injection signatures at the geosynchronous orbit. We used data from GOES-15 [135°W], GOES-14 [105°W], GOES-12 [75°W], and GOES-11 [135°W]. The GOES satellites were located between ~19 to 24 MLT for all STEVE events. The longitudinal difference of GOES-15 and GOES-11 with Athabasca is ~63 degree, whereas GOES-14 and GOES-12 is ~38 degree and 8 degree, respectively. In this paper, we have shown only particle data from GOES-15 to demonstrate the dispersionless injection prior to three STEVE events occurring during 2018-2019.

We have used the Space Physics Environment Data Analysis Software (SPEDAS) tool (Angelopoulos et al., 2019) to download and analyze the 1-min geomagnetic activity indices, ground-based magnetic field, and GOES particle flux data. We used median subtracted X-component magnetograms in this study.

3 Observations

We used ASI images and N-S keogram to identify the detachment of arcs based on visual inspection. Figure 1 shows the typical ASI images at red-line (630.0 nm) and green-line (557.7 nm) for red arc (upper panel A), red+green arc (middle panel B), and STEVE (bottom panel C). Spectrally pure red-line emission is considered as red arcs, not associated with simultaneous observation in the green-line (panel A). The arc in red-line with simultaneous emission in green-line is referred as red+green arc (panel B). STEVE is a narrow bright arc compared to normal red arc, exhibiting wavy structure along the arc, and sometimes also picket fence structure in the green-line (panel C).

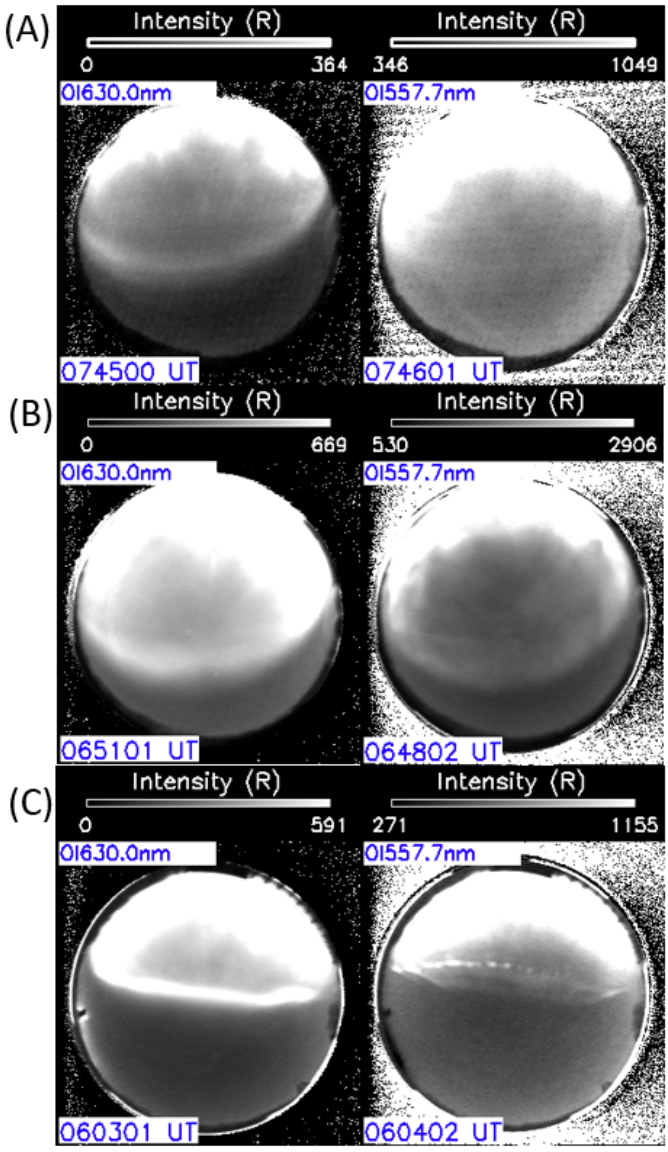

Figure 1: Typical all-sky images of red arc on September 17, 2017 (arc in 630.0 nm with no corresponding emission in 557.7 nm; upper panel A), red+green arc on May 14, 2015 (emission in both 630.0 nm and 557.7 nm; middle panel B), and STEVE on March 11, 2010 (bright arc in 630.0 nm and picket fence in 557.7 nm; bottom panel C).

Figure 2 shows a typical example of NS keogram for red-line (630.0 nm) and green-line (557.7 nm) for red arc (Event 1; upper panel A), red+green arc (Event 2; middle panel B), and STEVE (Event 3; bottom panel C). Before the

detachment of all arcs, the high-latitude aurora expands equatorwards. When the oval aurora returned to higher latitudes, an arc detached itself from the main auroral oval and moved further equatorward. This phenomenon is referred as detachment of arc from the main auroral oval as described by Takagi et al. (2018) for SAR arc and Yadav et al. (2021a) for STEVE. For red arc (Event 1), this detachment was observed at ~0740 UT in the red-line keogram. Although the equatorward extension of oval aurora is observed in the green-line keogram, arc detachment did not occur. For red+green arc (Event 2), the detachment of arc is observed in both the red-line and green-line keogram at ~0645 UT. A narrow and bright arc structure detaching itself from the main auroral oval at ~0615 UT is STEVE in the red-line (Event 3). By contrast, red arc appeared diffuse and wide (Event 1). For STEVE (Event 3), although 557.7 nm image shows the picket fence structure, the detachment of arc at ~0615 UT is not observed, like in the red-line.

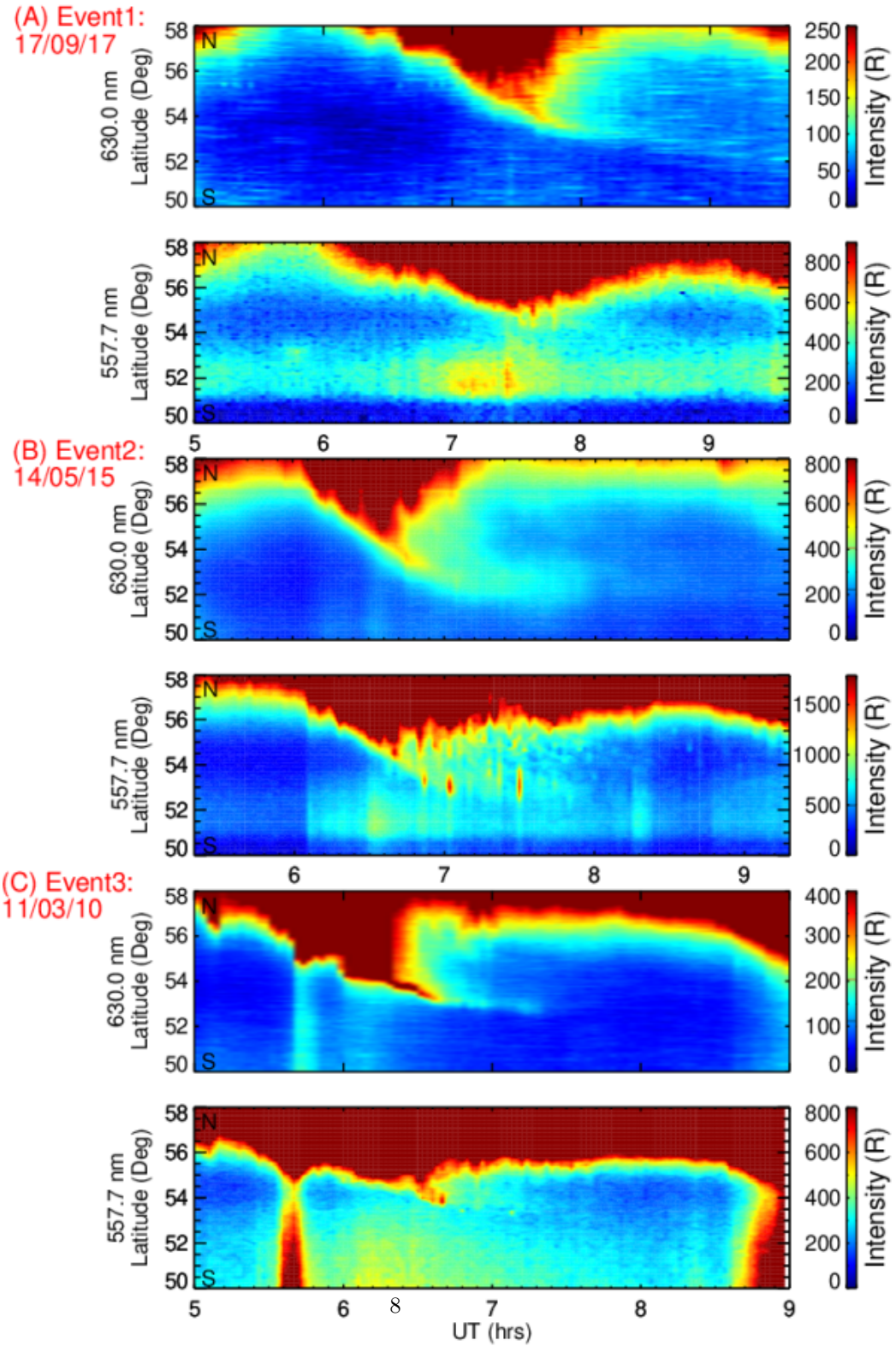
(A) Event1:
17/09/17
630.0 nm
557.7 nm
Latitude (Deg)
Intensity (R)
N
S
(B) Event2:
14/05/15
(C) Event3:
11/03/10
UT (hrs)

Figure 2: Typical NS keogram for red arc (Event 1), red+green arc (Event 2), and STEVE (Event 3).

For arc detachment statistics, first, the feature of arc detachment was identified from NS keograms by visual inspection. Then, we checked all-sky images to ensure that the features picked up from the keograms were east-west elongated arcs detaching from the main auroral oval. Only those arcs are considered which persisted at least 30 mins after their detachment from the main auroral oval. STEVE consists of continuum spectrum from 400-730 nm (Gilles et al., 2019). Therefore, although Figure 1 and 2 shows the STEVE emissions only in red- and green-line, the presence of STEVE is identified by using the images at all six filters including the "nominal background", except for the OH band, as described in Yadav et al. (2021a). The primary objective of this study is to examine the detachment rate. So, cases in which detachment was not observed were not considered. Since STEVE is a rare event, we have considered STEVE events even when the detachment was ambiguous.

Given the fact that the ASI measurements have limitation as observations cannot be made if the sky is cloudy, only those nights are considered for which at least 4-hour observation was present. After this restriction, the number of nights available to us for identifying the arc detachment were reduced to 948. In 948 nights of observations and 6376 hours of data, we identified 139 red arcs, 42 red+green arc, and 26 STEVE events. Note that Takagi et al. (2018) analyzed the total occurrence (from the detachment until the arc remained detectable in the ASI images) of SAR (red) arcs, whereas the present study is focused solely on the detachment rate of red arcs, red+green arcs, and STEVE.

STEVE does not invariably display the feature of detachment from the main auroral oval. Occasionally, STEVE is found to emerge at the equatorward boundary of diffuse emissions that had already expanded equatorward from the main auroral oval. Out of 26 STEVE events, the detachment from the main auroral oval was observed for 13 events. For 4 events, the feature of detachment was not clear either because of the absence of images or presence of clouds. For the remaining 8 events, STEVE developed at the equatorward boundary of the intense diffuse emission that expanded equatorward from the main auroral oval. Two examples of such events are shown in supplementary Figure S1.

3.1 Statistics of detachment rate

The 'detachment of arc per hour' is defined as the ratio between total number of detachment events and total hours of data. Figure 3 shows the yearly (2006-2020) rate of detachment for red, red+green arcs, and STEVE. The yearly averaged variation of solar wind speed (Vx), Ap index, and F10.7 is superposed to study the association of arc detachment with the solar and geomagnetic activity. In general, the detachment rate of red+green arcs exhibits dependence on geomagnetic activity with higher detachment rate when Ap and solar wind speed were high and no occurrence for low Ap and solar wind speed years (2009-2011 and 2020). However, the detachment rate of both red and red+green arcs

was low during 2016-2017 when the Ap index was the highest. Comparing the two solar minimum, the detachment rate of red arc was highest during 2018-2019 when both the solar wind and Ap index was at the higher levels as compared to 2008-2009. In comparison to red+green arcs, the detachment rate of red arcs was higher even for the lowest Ap years (2009-2010). These results suggest that the detachment rate of red and red+green arc exhibits dependence on both the geomagnetic activity (Ap and solar wind) and solar flux. The detachment of STEVE was maximum during the solar minimum year 2019, and then for 2010 and 2018. The high detachment rate of STEVE coincided with the high detachment rate of red arcs.

Figure 4 shows the detachment rate of red, red+green arcs, and STEVE as a function of MLT. The MLT distribution of detachment rate was calculated for each arc-type separately by dividing the total events observed in a particular 2-hour time slot to the total number of arc events. In general, the detachment rate of all arcs exhibits asymmetric distribution with highest rate in the premidnight sector. For STEVE, detachment rate is highest at 22-24 MLT, and then at 20-22 MLT, before midnight. The detachment rate of red and red+green arcs maximized around midnight, that is at 22-24 and 00-02 MLT.

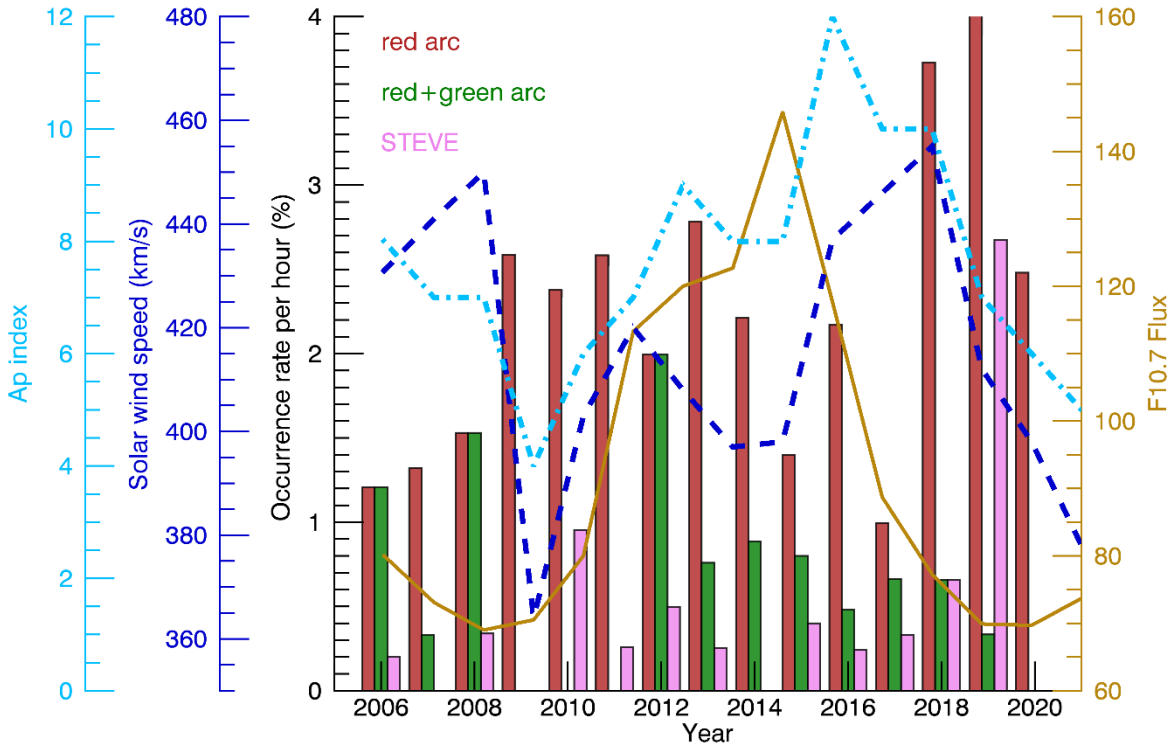

Figure 3: The yearly (2006-2020) variation of rate of detachment for red arc, red+green arc, and STEVE. Blue dashed, cyan dashed dot, and solid gold color curve represent the yearly averaged variation of solar wind speed (Vx), Ap index, and F10.7.

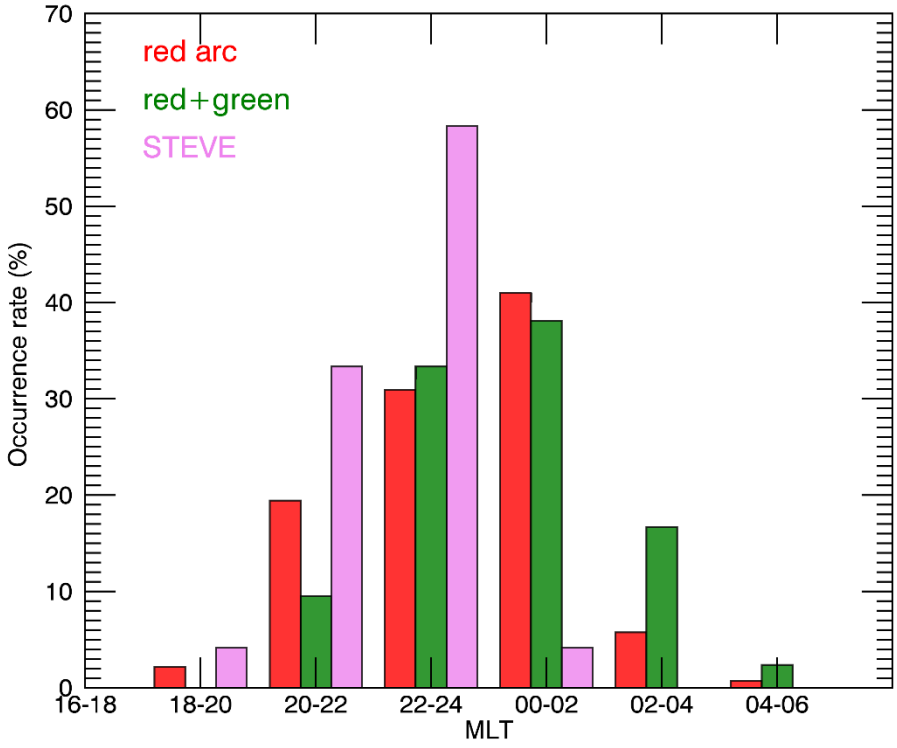

Figure 4: The detachment rate of red a rc, red+green arc, and STEVE as a function of MLT.

3.2 Superposed epoch analysis

In order to understand the specific geomagnetic activity during which subauroral arcs detached as red arc, red+green arc, and STEVE, we perform the superposed epoch analysis for different geomagnetic activity indices from 3 hr before to 3 hr after the detachment event. Note that the superposed epoch analysis of AL-index and SYM-H index for STEVE (Gallardo-Lacourt et al., 2018) and SAR arc (Takagi et al., 2018) has been already reported. These studies highlighted that both STEVE and SAR arc occurred at the end of expansion phase or just at the beginning of recovery phase. In the following subsections, we compare the results of superposed epoch analysis of different geomagnetic activity indices for three different types of arcs.

3.2.1 AL index

Figure 5 shows the results of superposed epoch analysis of AL index from 3 hr before to 3 hr after the detachment of (a) red arcs, (b) red+green arc, and (c) STEVE. The vertical dashed line at zero hour represents the time of detachment of arcs as detected in the optical data. The average values defined every 1-min for red arc, red+green arc, and STEVE are shown by red, green, and purple curve, respectively. The grey lines show the standard deviation. The AL index began to decrease ~1 hr prior to the detachment of all arcs. Compared to the values 1-hr prior to the detachment, the AL-index exhibits a decrease of ~ 250 nT for STEVE, ~130 nT for red and red+green arc. The detachment of arcs occurred towards the end of expansion phase and beginning of recovery phase. Unlike red and red+green arc, the AL index for STEVE shows the presence of small perturbations around the end of expansion phase. In order to investigate this aspect in detail, we made the superposed epoch analysis using X-component magnetogram at FSMI, enable focusing on the detachment of arc with respect to auroral-zone substorm activity in the longitude of Athabasca ASI.

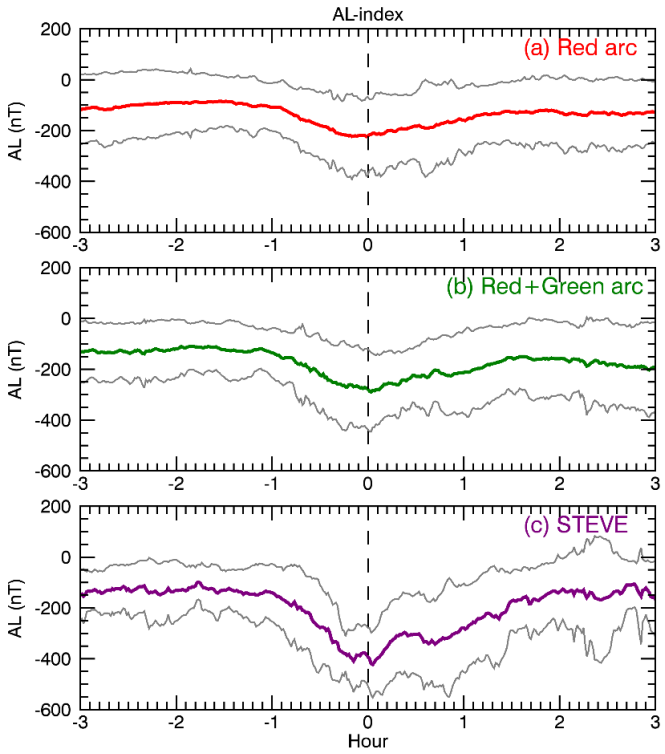

Figure 5: Superposed epoch analysis of (a) red arc (139 events), (b) red+green arc

(42 events), and (c) STEVE (26 events). The vertical dashed line at zero hour represents the time of detachment of arcs as detected in the optical data. The average values defined every 1-min for red arc, red+green arc, and STEVE are shown by red, green, and purple curve, respectively. The grey lines show the standard deviation.

3.2.2 X-component magnetogram at Fort Smith

Figure 6 is same as Figure 5 but for X-component magnetogram at FSMI. In general, for all arcs, the X-component magnetic field at FSMI began to decrease 1 hr prior to the time of arc detachment, with its minimum value occurring around the detachment time. On average, the X-component magnetogram decreased ~300 nT for STEVE, ~200 nT for red+green arcs, and ~100 nT for red arcs. The X-component magnetogram at FSMI displayed perturbations in the recovery phase of the substorms during STEVE detachment, not observed for other arcs. STEVE detachment coincided with a sharp recovery from the expansion phase and start of additional activity in the recovery phase of a substorm. By analyzing three STEVE events, Yadav et al. (2021) also reported the association of STEVE with additional activities in the recovery phase of a substorm by using X-component magnetogram at FSMI for three STEVE events.

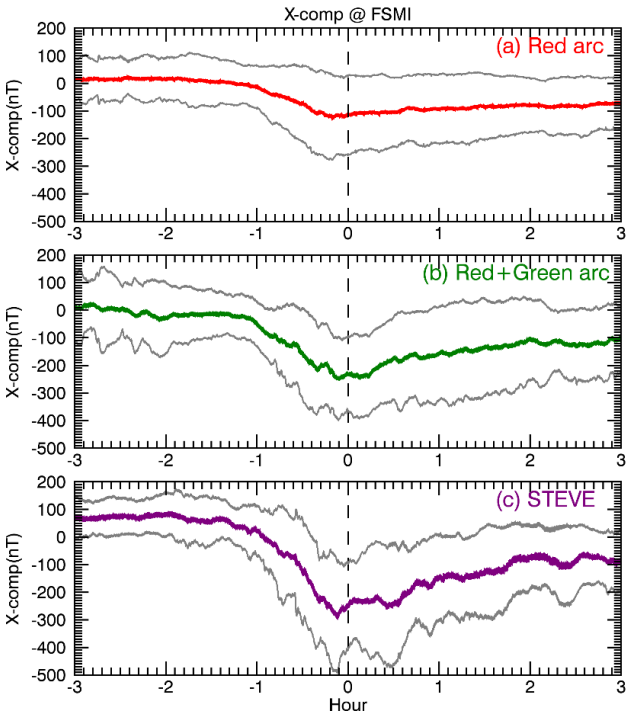

Figure 6: Same as Figure 5 but for X-component magnetogram at Fort Smith (FSMI).

3.2.3 X-component magnetogram at Athabasca

We also perform the superposed epoch analysis for the X-component magnetogram at Athabasca, shown in Figure 7. The X-component magnetogram at Athabasca began to decrease ~1 hr before the detachment of red arc and red+green arc. For STEVE, X-component magnetogram at Athabasca showed a hump of slight (~10 nT) enhancement ~30-minutes prior to the detachment followed by a decrease. Such feature is not observed for red arc and red+green arc. The maximum decrease prior to detachment was ~40 nT for STEVE and red+green arc and 20 nT for red arc.

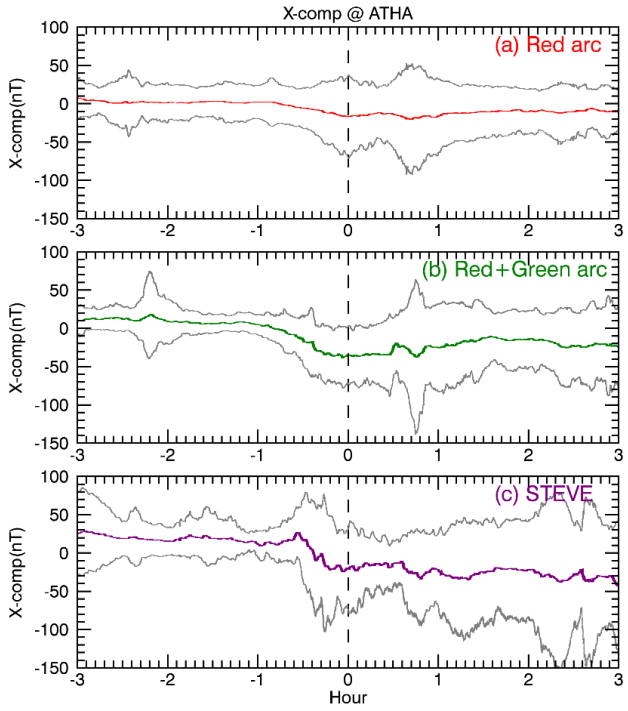

Figure 7: Same as Figure 5 but for X-component magnetogram at Athabasca (ATHA).

3.2.4 SYM-H index

Figure 8 shows the superposed epoch analysis for the SYM-H index. Takagi et al. (2018) reported no clear change in the SYM-H index before or after the detachment of SAR arcs. Similarly, the SYM-H index shows no change before and after the detachment of both red and red+green arcs. Unlike other arcs, the SYM-H index exhibits slight variations before and after the detachment of STEVE. The SYM-H index shows the hump of slight enhancement just prior to the detachment of STEVE. The hump is followed by a gradual decrease with the minimum values occurred 1 hr after the detachment of STEVE. The minimum value of the SYM-H index remains near -15 nT for red arcs, -20 nT for red+green arcs, and -25 nT for STEVE events. This indicates that STEVE likely to occur during relatively geomagnetically disturbed periods with more developed ring current as compared to red and red+green arcs.

3.2.5 ASY-H index

Figure 9 shows the superposed epoch analysis for the ASY-H index. In general,

the ASY-H index began to increase gradually ~1 hour before the arc detachment for all arcs. For STEVE, the ASY-H index showed an abrupt enhancement ~30 mins before the detachment, exhibiting a prominent bay-like structure. The ASY-H index shows an enhancement of 20 nT for STEVE and 5 nT for red and red+green arc. The detachment of arcs occurred immediately after the peak in ASY-H index for all arcs. The maximum magnitude of ASY-H index was ~45 nT for STEVE, 25 nT for red and red+green arc. Thus, bay-like enhancement in the ASY-H index is significantly prominent for STEVE as compared to red and red+green arc. Although the magnitude of ASY-H index for red arc and red+green is same, the bay-like feature of ASY-H appeared prominently for red arc in comparison to red+green arc. The prominent bay-like ASY-H increase for STEVE probably indicates the connection of asymmetric ring current to the generation of STEVE during the substorm expansion phase.

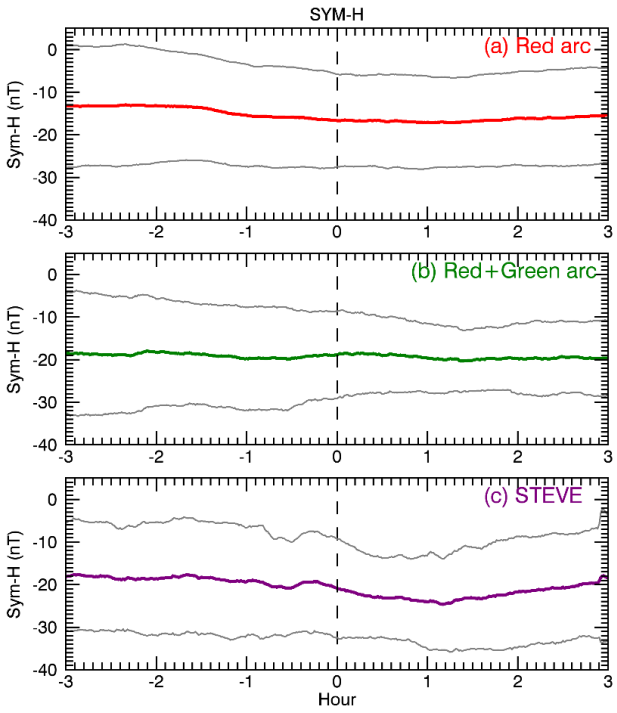

Figure 8: Same as Figure 5 but for SYM-H index.

3.2.6 X-component magnetogram at Boulder

In order to examine the local substorm activity, we also performed the similar analysis for H-component magnetogram at Boulder (BOU), shown in Figure

10. Although there is around 1-hr time difference from Boulder and Athabasca, the magnetic field variation at Boulder might provide an estimate of the middle latitude variation of X-component magnetogram at the longitude zone of Athabasca. Similar to the ASY-H index, the X-component magnetogram at Boulder began to increase gradually 1-hr prior to the arc detachment for all arcs; however, an abrupt increase ~30-mins prior to the detachment is observed only for STEVE. The X-component magnetogram exhibits an enhancement of ~20 nT for STEVE. By contrast, the enhancement of X-component magnetogram was gradual, broad, and weak (~10 nT) for red arc and very weak for red+green arc (~3 nT). Thus, the mid-latitude positive bay occurred prominently for STEVE as compared to red and red+green arc. The detachment of all arcs occurred immediately after the appearance of positive bay structure.

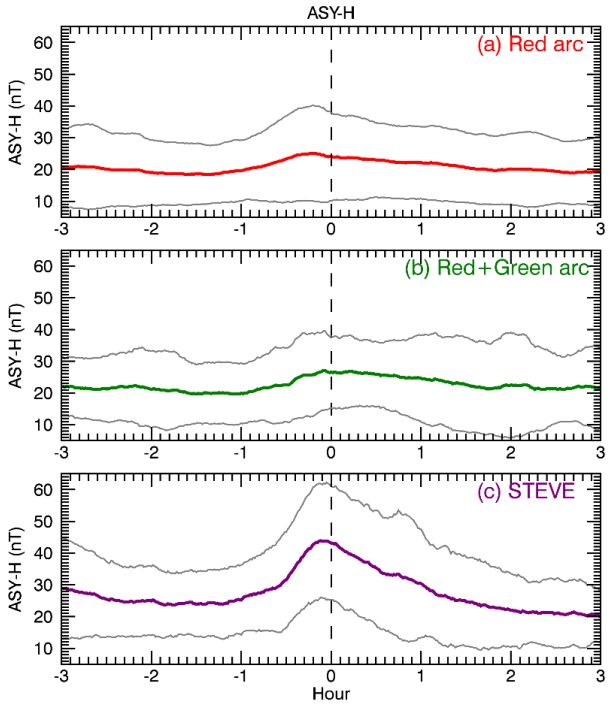

Figure 9: Same as Figure 5 but for ASY-H index.

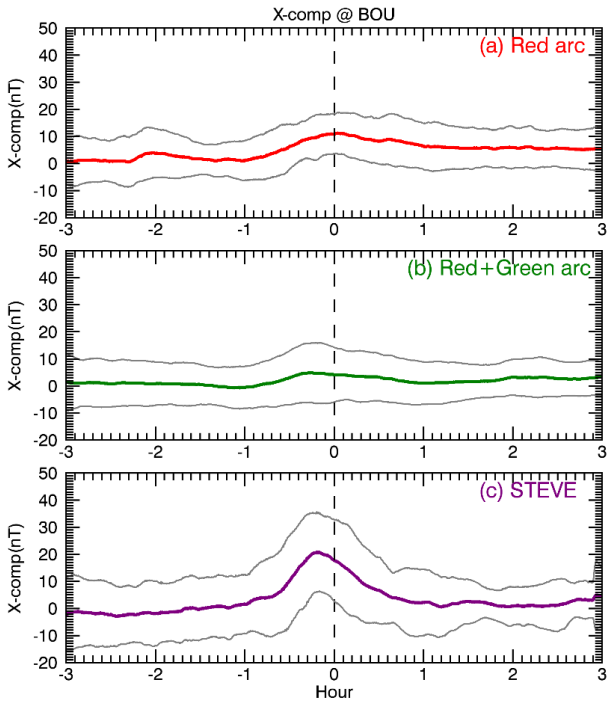

Figure 10: Same as Figure 5 but for X-component magnetogram at Boulder (BOU).

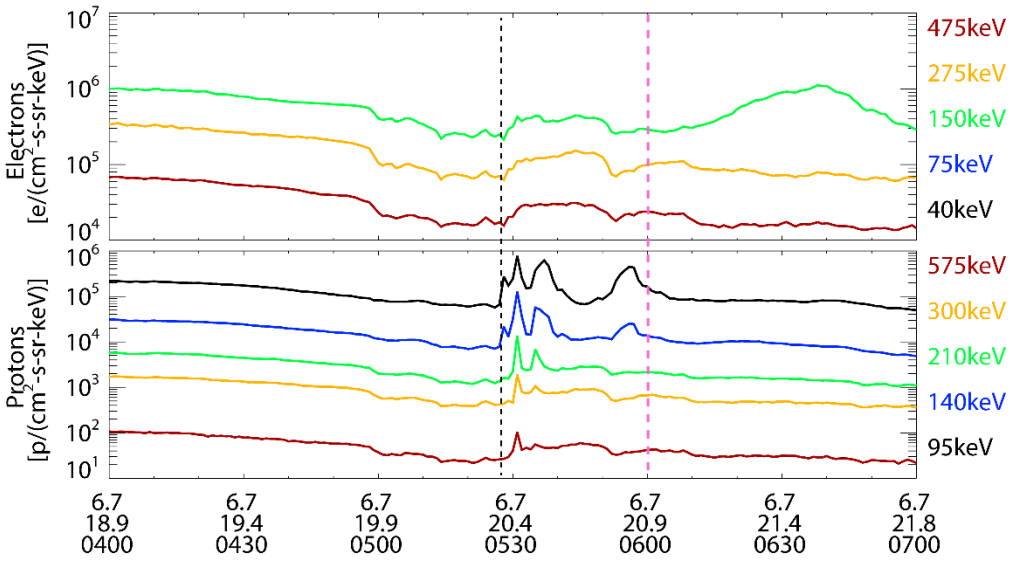
Electrons
[e/(cm²-s-sr-keV)]
Protons
[p/(cm²-s-sr-keV)]
475keV
275keV
150keV
75keV
40keV
575keV
300keV
210keV
140keV
95keV
L-shell
MLT
hhmm
2018 Aug 18
6.7 6.7 6.7 6.7 6.7 6.7 6.7
18.9 19.4 19.9 20.4 20.9 21.4 21.8
0400 0430 0500 0530 0600 0630 0700

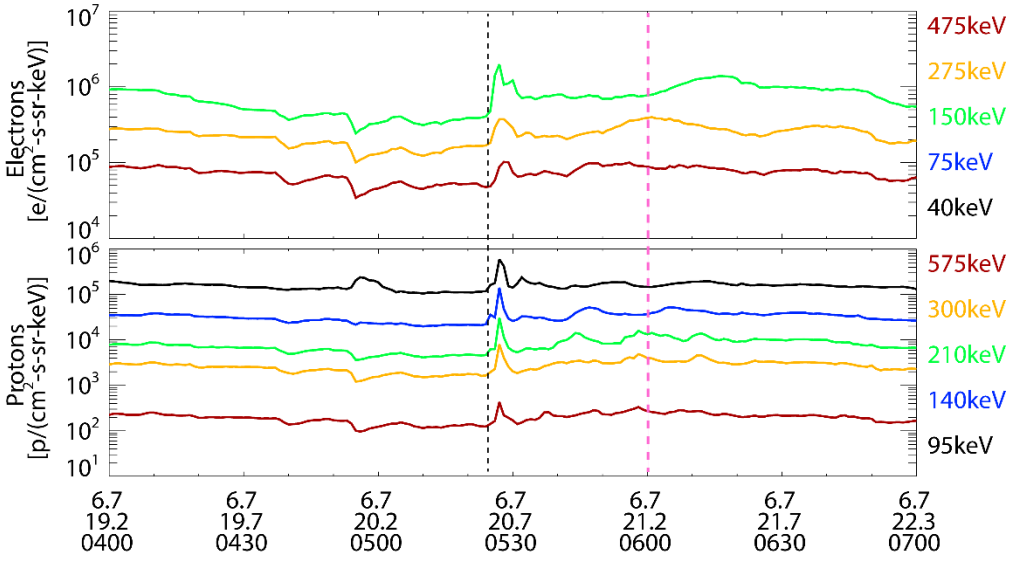
Electrons
[e/(cm²-s-sr-keV)]
Protons
[p/(cm²-s-sr-keV)]
475keV
275keV
150keV
75keV
40keV
575keV
300keV
210keV
140keV
95keV
L-shell
MLT
hhmm
2019 Mar 02
6.7 6.7 6.7 6.7 6.7 6.7 6.7
19.2 19.7 20.2 20.7 21.2 21.7 22.3
0400 0430 0500 0530 0600 0630 0700

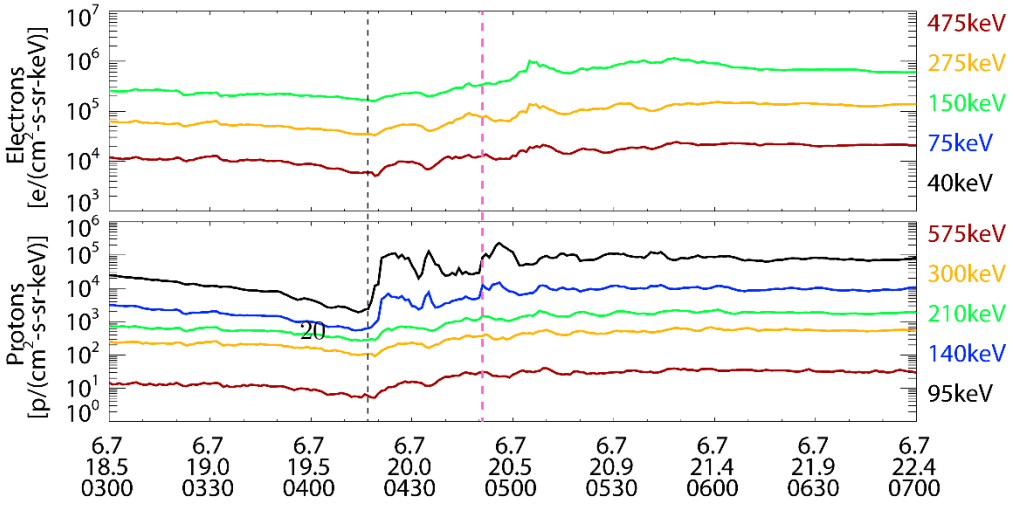
Electrons
[e/(cm²-s-sr-keV)]
Protons
[p/(cm²-s-sr-keV)]
475keV
275keV
150keV
75keV
40keV
575keV
300keV
210keV
140keV
95keV
L-shell
MLT
hhmm
2019 May 02
6.7 6.7 6.7 6.7 6.7 6.7 6.7 6.7 6.7
18.5 19.0 19.5 20.0 20.5 20.9 21.4 21.9 22.4
0300 0330 0400 0430 0500 0530 0600 0630 0700

Figure 11: Examples of energetic electron and proton flux as a function of L-value, MLT, and UT for three STEVE events obtained from GOES-15 spacecraft. The interval of dispersionless enhancement is highlighted by black dashed lines. The purple dashed line represent the approximate time of STEVE detachment observed in the all-sky images.

3.3 Linkage of STEVE with substorm activity

We analyzed the GOES spacecraft magnetic field and particle flux data to identify the substorm associated injection at the geostationary orbit for STEVE events. Interestingly, we found that most of the STEVE events (20 events) were accompanied by the substorm associated injection at the geostationary orbit approximately 30 mins prior to the detachment of STEVE. Although we have used different GOES spacecrafts to identify the feature of diapolarization and substorm associated injection for all 26 STEVE events spanning from 2006 to 2019, here we have shown only three examples using GOES-15 particle flux (both electron and proton) data. Figure 11 shows three examples of energetic electron and proton fluxes from GOES-15 spacecraft as a function of L-value, MLT, and UT for STEVE events of (A) 18 August 2018, (B) 02 March 2019, and (C) 02 May 2019. GOES-15 was in the premidnight sector at 2000 MLT for these three events. The longitudinal difference of GOES-15 and Athabasca ASI is ~63 degree. The detachment time of STEVE arc is highlighted by purple dashed line, as observed in the red-line ASI images at Athabasca. The black dotted lines indicate the start of dispersionless enhancement for both electron and proton fluxes. The dispersionless enhancement with a simultaneous increase of the electron (by a factor of ~1.5-3.0) and ion fluxes (by a factor of ~2 to an order of magnitude) at ~0527-0552 UT was observed on 18 August 2018 (A) and STEVE started at 0600 UT. Similarly, at 0525-0532 UT, dispersionless enhancement by a factor of ~4 was observed for 02 March 2019 (B) and STEVE observed at 0600 UT. For the event of 02 May 2019, STEVE began at 0450 UT and the dispersionless enhancement by a factor of ~2-4 was observed at ~0415-0435 UT. The enhancement of proton flux was found to be around one order of magnitude higher for lower energies (95 and 140 keV) for 02 May 2019 (C). Since GOES-15 observes near simultaneous dispersionless injections for both protons and electrons, the location of the injections must be close to the location of GOES-15 at 2000 MLT. GOES particle flux data confirm substorm onset before the STEVE events. Although not shown here, the events of diapolarization and substorm associated injection were also observed for red and red+green arcs.

4 Discussion

Based on 15-years of ASI data at Athabasca, we present a detailed comparative study on the occurrence characteristics of arc detachment from the main auroral oval for three different types of subauroral arc: pure red arc, red+green emission arc, and STEVE. Using monochromatic images at six different wavelengths, we identified 139 red arcs, 42 red+green arcs, and 26 STEVE events. The pure reds arcs observed in this study may be closely related to traditional SAR arcs (Takagi et al., 2018). However, we are not referring pure red arcs as

SAR arc because of the association of red arcs with subauroral ionospheric drift (SAID) (Sazykin et al., 2002) and particle precipitation from the plasma sheet particularly in the midnight sector (Yadav et al., 2021b; under communication).

Covering two solar minimum periods, our results revealed that the detachment rate of red arcs was maximum during solar minimum and higher geomagnetic activity conditions. The geomagnetic activity (both solar wind and Ap index) were higher in 2019-2020 as compared to 2008-2009. Likewise, detachment rate of red arcs was higher in 2019-2020 as compared to 2008-2009. In comparison to red+green arcs, the detachment rate of red arcs was higher even for the lowest Ap years (2009-2010). The detachment rate of STEVE also maximized in solar minimum and high-geomagnetic activity year (2019). The red+green arc showed no occurrence or had minimum occurrence during low Ap and low solar wind speed years (2009-2011 and 2020). The detachment rate of both red and red+green arcs was low during the years of highest geomagnetic activity (2016-2017). Takagi et al. (2018) reported that the occurrence rate of SAR arc detachment was low in the solar maximum and minimum and high during the period of increase or decrease of solar activity. Alexeyev et al. (2009) also showed that the occurrence rate of SAR arcs has a maximum in the declining phase of solar activity. These studies also reported that the occurrence rate of SAR arcs correlated well with the geomagnetic activities represented by the Ap index. Note that both of these studies were based on nearly one-solar cycle data, whereas, 15-years of data used in the present study provides us a distinct opportunity to compare two solar minimum periods. Our results indicate that the detachment rate of red and red+green arc has dependence not only on geomagnetic activity but also on the solar flux.

It is well-known that the boundary of auroral oval expands with increasing geomagnetic activity, that is, the auroral zone expands equatorward at times of enhanced geomagnetic period. Thus, during high geomagnetic activity period, observed in 2016-2017, there is a high possibility that the auroral oval expands to reach latitudes of Athabasca. The magnetic latitudes of SAID is also known to shift equatorward with increasing geomagnetic activities (Karlsson et al., 1998; He et al., 2014). This implies that the probability of appearance of subauroral arc should be reduced at the latitudes of Athabasca during higher geomagnetic activity, but at the same time, should have higher occurrence at lower latitudes. Mendillo et al. (2016) by analyzing 27-years of ASI data at Millstone Hill [42.6°N, 288.5°E, 56° invariant latitude] reported that occurrence of SAR arcs was minimum during solar minimum years and maximum during solar maximum years, opposite to what we observe at Athabasca.

We presented the magnetic local time (MLT) distribution of red, red+green arcs, and STEVE. STEVE is found to occur predominantly in the premidnight sector (highest occurrence at 22-24 MLT, and then at 20-22 MLT). Using THEMIS ASI and REGO database Gallardo-Lacourt et al. (2018) identified 28 STEVE events between 22 and 01 MLT. A large majority of SAID occurred in the premidnight sector (2000-2300 MLT) with strength being higher for events close

to 2200 MLT (Karlsson et al., 1998; Figueiredo et al., 2004). Being an optical manifestation of SAID (MacDonald et al., 2018; Archer et al., 2019), STEVE showed good correlation with the occurrence characteristics of SAID. Red and red+green arcs exhibit maximum detachment rate around the midnight sector (highest occurrence at 00-02 MLT, and then at 22-24 MLT). Using Athabasca ASI (2006-2016), Takagi et al. (2018) reported that the occurrence rate of SAR arc detachment was highest in the premidnight sector (20–22 MLT). They suggested that the detachment of SAR arcs may correspond to the dynamical injection of ring current ion populations into the inner magnetosphere. Note that the study of Takagi et al. (2018) is different from the present study because they considered the total occurrence rate (from the time of detachment till until the arc remained detectable in the ASI images) of SAR arcs, whereas we have focused solely on the detachment rate. In addition, Takagi et al. (2018) perceived STEVE events as the SAR arc. In the present study, highest detachment rate of red and red+green arcs is observed around the midnight sector, suggesting that the low-energy particle (<10 keV) precipitation from plasma sheet might also play a role in the formation of subauroral arcs around the midnight sector (Yadav et al., 2021b; under communication).

In section 3.2, we performed superposed epoch analysis to compare various geomagnetic activity indices during the detachment of red, red+green arcs, and STEVE. Results reveal that STEVE occurred during higher geomagnetic activity as compared to that observed for red and red+green arcs. Gallardo-Lacourt et al. (2018) reported that STEVE occurred at the end of a prolonged substorm expansion phase (~60 min). However, our results show that the substorm expansion phase persisted for ~60 mins (both in AL index and X-component magnetogram) not only for STEVE but also for red and red+green arcs. The notable point is that substorm intensities estimated by the magnetic field variations were ~2-3 times higher for STEVE as compared to red and red+green arcs.

In general, all arcs occurred towards the end of expansion phase and beginning of recovery phase, as already shown in the earlier studies for STEVE (Gallardo-Lacourt et al. 2018) and SAR arcs (Takagi et al., 2018). The X-component magnetogram at Fort Smith indicated that the detachment of STEVE coincided with the sharp recovery from the expansion phase and the beginning of additional activity in the recovery phase of a substorm. Based on three STEVE events, Yadav et al. (2021a) first highlighted the association of STEVE detachment and brightness with the additional activities in the recovery phase of a substorm. Our results, based on 26 STEVE events, provide further credence to the findings of Yadav et al. (2021a) that triggering of STEVE requires additional energization, observed in terms of additional activities in the recovery phase of a substorm. Gallardo-Lacourt et al. (2018) identified streamers within the auroral oval for STEVE events, indicating the association of STEVE with substorm activity.

Our results, for the first time, show the association of STEVE with ASY-H

index in terms of a prominent bay-like enhancement just prior to the detachment of STEVE. The detachment of STEVE occurred immediately after the peak in ASY-H index. A sharp bay-like enhancement is also observed for X-component magnetogram at Boulder, a mid-latitude station in the longitude zone of Athabasca. The ASY-H index is associated with an intensification of asymmetric ring current in the dusk sector (Nishida, 1978). The bay-like variations of H- and D-components might indicate the onset of substorm expansion (Rostoker et al., 1980). Although the bay-like enhancement is also observed for the red and red+green arcs, it was weak (5 nT) and broad compared to STEVE (20 nT). The association of SAR arc with a bay-like structure in the ASY-H index is shown in the past studies (e.g., Ievenko et al., 2008). Unlike red arcs, a clear bay-like structure prior to the detachment of arc is not observed for green+red arc, indicating that the mechanism for the formation of red+green arc may be different from the red arc. It is notable that positive bay enhancement in ASY-H index for STEVE was 4 times stronger than red and red+green arcs. This suggests the strong association of STEVE with the asymmetry in ring current.

Lastly, in order to further provide evidence to the association of STEVE with substorms, we analyzed GOES particle flux. Results unveil that majority (20/26) of the STEVE events were accompanied by the dispersionless injection of both electron and proton flux at geosynchronous orbit, a ubiquitous characteristic of substorms. Such enhancements were observed ~30 mins prior to the detachment of STEVE into the nightside. Note that such particle injection events at the geostationary orbit were also observed often for red and red+green arcs. The dispersionless injection of both electron and proton flux at geosynchronous orbit for SAR arc was reported in the past (e.g., Ievenko et al., 2008). However, the peculiar features in the magnetic field was observed only for STEVE, for example, i) both ASY-H index and X-component magnetogram at Boulder showed an abrupt enhancement ~30-mins prior to the STEVE arc detachment, forming a feature of prominent positive bay-like enhancement before the detachment of STEVE arc ii) the SYM-H index and X-component magnetogram at Athabasca showed small enhancement ~30 mins prior to the detachment of STEVE, and iii) the X-component magnetogram at Fort Smith shows the presence of additional activities in the recovery phase of substorms. Such features were not observed for red arcs and red+green arcs. These results unambiguously indicate that STEVE develops after the substorm associated energy injection and consequent intensification of asymmetric ring current.

5 Conclusions

While individual statistics of SAR arc and STEVE have been reported in previous studies, here we present for the first time comparative statistical study of three types of subauroral arc from the same station—an aspect not yet addressed. We have used 15-years (2006-2020; covering two solar minimum) of ASI observation at Athabasca to perform a comparative statistical study of red arcs, red+green arcs, and STEVE. The most commonly observed arc was red

arc (139 events), followed by red+green arc (42 events) and STEVE (26 events), an extremely rare phenomenon.

We found that the detachment rate of red arcs was high for the solar minimum and high geomagnetic activity years, displaying dependence on both solar flux and geomagnetic activity. The detachment rate of red+green arc was higher for moderate geomagnetic activity years and had minimal or no occurrence for low geomagnetic activity. The detachment rate of STEVE also maximized in solar minimum and high-geomagnetic activity year (2019). Given that auroral oval expands equatorward with increasing geomagnetic activity, the occurrence of all subauroral arcs was low during peak geomagnetic activity year (2016-2017), indicating that occurrence rate of arcs has a dependence on the location of observing station. The detachment rate of STEVE was higher in the premidnight sector, whereas red arcs and red+green arcs exhibit higher detachment rate around the midnight sector.

In order to provide insights on the specific geomagnetic conditions during STEVE, we performed a comparative superposed epoch analysis for various geomagnetic activity indices for red arcs, red+green arcs, and STEVE. Results reveal that STEVE occurred during relatively higher geomagnetic activity, the substorm activity was ~2-3 times higher for STEVE as compared to other arcs. The ASY-H index shows the prominent bay-like enhancement with a peak just prior to the detachment of STEVE, the bay-like enhancement was ~4 times higher for STEVE as compared to other arcs.

Majority of STEVE events were accompanied by the feature of dispersionless injection for both electron and proton flux at the geosynchronous orbit ~30 mins prior to the STEVE detachment. The feature of dispersionless injection for particle flux at the geosynchronous orbit was also observed for red arcs and red+green arcs. However, the geomagnetic activity indices show peculiar features for STEVE and not for other arcs. For example, i) both ASY-H index and X-component magnetogram at Boulder showed the presence of prominent positive bay-like enhancement before the detachment of STEVE, ii) the SYM-H index and X-component magnetogram at Athabasca showed small enhancement ~30 mins prior to the STEVE detachment, and iii) the X-component magnetogram at Fort Smith and AL index showed the presence of additional activities during the time of STEVE detachment. The development of STEVE occurred at the end of substorm expansion phase and significant intensification of asymmetric ring current in the dusk sector.

Acknowledgement

- The all-sky imager data at Athabasca are available through ISEE/Nagoya University. Quick-look plots of the OMTI data are available at http://stdb2.isee.nagoya-u.ac.jp/omti/ and the data can be accessed from the ERG Science Center operated by ISAS/JAXA and ISEE/Nagoya University (https://ergsc.isee.nagoya-u.ac.jp/data/ergsc/ground/camera/omti/asi/).
- The all-sky imager at Athabasca was calibrated using optical facilities of

National Institute of Polar Research, Japan (Ogawa et al., 2020). It is housed in facilities developed and supported by the Canada Foundation for Innovation.

- The solar wind data and geomagnetic activity indices (both one-minute and one-year resolution) were obtained from the SPDF, NASA, USA (http:// omniweb.gsfc.nasa.gov)
- The GOES spacecraft magnetic field and particle data from magnetic field (MAG), MAGnetospheric Electron Detector (MAGED) and MAGnetospheric Proton Detector (MAGPD) were provided by the NOAA National Geophysical Data Center (https://satdat.ngdc.noaa.gov/sem/goes/data/).
- Ground-based magnetic field data is the part of following networks. Athabasca (ATHA) data from this period was part of the AUTUMN network operated by Athabasca University. Fort Smith (FSMI) is part of CARISMA (Mann et al., 2008) network. We thank I.R. Mann, D.K. Milling and the rest of the CARISMA team for data. CARISMA is operated by the University of Alberta, funded by the Canadian Space Agency. Boulder (BOU) is a part of the US Geological Survey network. Original data provided by the USGS Geomagnetism Program (http://geomag.usgs.gov). All the magnetic field data are downloaded from the THEMIS website (http://themis.ssl.berkeley.edu/data/themis/thg/mirrors/mag/).
- We have used the Space Physics Environment Data Analysis Software (SPEDAS) tool (Angelopoulos et al., 2019) to download and analyze the 1-min geomagnetic activity indices, ground-based magnetic field, and GOES particle flux data.
- This work is supported by JSPS KAKENHI (16403007, 19403010, 20244080, 23403009, 25247080, 15H05815, and 16H06286).

References

Anger, C. D., Moshupi, M. C., Wallis, D. D., Murphree, J. S., Brace, L. H., & Shepherd, G. G. (1978). Detached auroral arcs in the trough region. *Journal of Geophysical Research*, 83(A6), 2683–2689. https://doi.org/10.1029/JA083iA06p02683

Angelopoulos, V. et al. (2019), The Space Physics Environment Data Analysis System (SPEDAS). *Space Science Review*, 215. https://doi.org/10.1007/s11214-018-0576-4.

Alexeyev, V., Ievenko, I., & Parnikov, S. (2009). Occurrence rate of SAR arcs during the 23rd solar activity cycle. *Advances in Space Research*, *44*, 524–527. https://doi.org/10.1016/j.asr.2009.04.024

Archer, W. E., Gallardo-Lacourt, B., Perry, G. W., St-Maurice, J.-P., Buchert, S. C., & Donovan, E. F. (2019). Steve: The optical signature of intense subauroral

ion drifts. *Geophysical Research Letters*, *46*, 6279–6286. https://doi.org/10.1029/2019GL082687

Barbier, D. (1958). The auroral activity at low latitudes. *Annals of Geophysics*, 1, 4334–4355.

Chu, X., Malaspina, D., Gallardo-Lacourt, B., Liang, J., Andersson, L., Ma, Q., et al (2019), Identifying STEVE's Magnetospheric Driver Using Conjugate Observations in the Magnetosphere and on the Ground. *Geophysical Research Letters,* 46. https://doi.org/10.1029/2019GL082789

Cornwall, J. M., Coroniti, F. V., & Thorne, R. M. (1971), Unified theory of SAR arc formation at the plasmapause. *Journal of Geophysical Research*, 76, 4428–4445. https://doi.org/10.1029/JA076i019p04428

Cole, K. (1965), Stable auroral red arcs, sinks for energy of Dst main phase. *Journal of Geophysical Research*, 70, 1689–1706, doi:10.1029/JZ070i007p01689.

Figueiredo, S., T. Karlsson, and G. T. Marklund (2004), Investigation of subauroral ion drifts and related field-aligned currents and ionospheric Pedersen conductivity distribution, *Annales Geophysicae*, 22, 923–934

Frey, H. U. (2007). Localized aurora beyond the auroral oval. *Reviews of Geophysics,* 45(1), 1003. https://doi.org/10.1029/2005RG000174

Gallardo-Lacourt, B., Nishimura, Y., Donovan, E., Gillies, D. M., Perry, G. W., Archer, W. E., et al. (2018). A statistical analysis of STEVE. *Journal of Geophysical Research: Space Physics,* 123, 9893–9905. https://doi.org/10.1029/2018JA025368

Gallardo-Lacourt, B., Frey, H.U. & Martinis, C. (2021). Proton Aurora and Optical Emissions in the Subauroral Region. *Space Science Reviews,* 217, 10. https://doi.org/10.1007/s11214-020-00776-6

Galperin, Y., Ponomarev, V. N., and Zosimova, A. G. (1974). Plasma convection in the polar ionosphere, *Annales Geophysicae*, 30, 1.

Gillies, D. M., Donovan, E., Hampton, D., Liang, J., Connors, M., Nishimura, Y., et al. (2019). First observations from the TREx Spectrograph: The optical spectrum of STEVE and the Picket Fence phenomena. *Geophysical Research Letters*, 46, 7207–7213. https://doi.org/10.1029/2019GL083272

Hoch, R. J., Stable auroral red arcs, *Reviews of Geophysics*, 11, 935, 1973.

He, F., X.-X. Zhang, and B. Chen (2014), Solar cycle, seasonal, and diurnal variations of subauroral ion drifts: Statistical results, *Journal of Geophysical Research: Space Physics*, 119, 5076–5086, doi:10.1002/2014JA01980

Inaba, Y., Shiokawa, K., Oyama, S., Otsuka, Y., Connors, M., Schofield, I., et. al. (2021). Multi-event analysis of plasma and field variations in source of stable auroral red (SAR) arcs in inner magnetosphere during non-storm-time sub-

storms. *Journal of Geophysical Research: Space Physics*, 126, e2020JA029081. https://doi.org/10.1029/2020JA029081

Ievenko, I.B., Parnikov, S.G., Alexeyev, V.N. (2008). Relationship of the diffuse aurora and SAR arc dynamics to substorms and storms, *Advances in Space Research*, 41, 8, 1252-1260

Karlsson, T., G. T. Marklund, and L. G. Blomberg (1998), Subauroral electric fields observed by the Freja satellite: A statistical study, *Journal of Geophysical Research*, 103(A3), 4327–4314, doi:10.1029/97JA00333.

Kozyra, J. U., E.G. Shelly, R. H. Comfort, L. H. Brace, T. E. Cravens, and A. F. Nagy, The role of ring current O + in the formation of stable red arcs, *Journal of Geophysical Research*, 92, 7487, 1987.

Kozyra, J. U., & Nagy, A. F. (1997), High-altitude energy source(s) for stable auroral red arcs. *Reviews of Geophysics*, 35, 155-190, 96RG03194.

MacDonald, E. A., Donovan, E., Nishimura, Y., Case, N. A., Gillies, D. M., Gallardo-lacourt, B., et al. (2018). New science in plain sight: Citizen scientists lead to the discovery of optical structure in the upper atmosphere. *Science Advances*, 4(March), 16–21. https://doi.org/10.1126/sciadv.aaq0030

Mann, I. R., et al. (2008). The upgraded CARISMA magnetometer array in the THEMIS era, *Space Science Review*, 141, 413–451, doi:10.1007/s11214-008-9457-6.

Moshupi, M. C., Anger, C. D., Murphree, J. S., Wallis, D. D., Whitteker, J. H., Brace L. H. (1979), Characteristics of trough region auroral patches and detached arcs observed by Isis 2. *Journal of Geophysical Research: Space Physics*, 84 (A4), 1333-1346. https://doi.org/10.1029/JA084iA04p01333

Mendillo, M., Baumgardner, J., & Wroten, J. (2016). SAR arcs we have seen: Evidence for variability in stable auroral red arcs. *Journal of Geophysical Research: Space Physics*, 121(1), 245–262. https://doi.org/10.1002/2015JA021722

Nagy, A. F., Roble, R. G., & Hays, P. B. (1970). Stable mid-latitude red arcs: Observations and theory. *Space Science Reviews*, 11, 709–727. https://doi.org/10.1007/BF00177029

Nishida, A. (1978). Geomagnetic Diagnosis of the Magnetosphere. *Springer, New York*.

Sazykin, S., Fejer, B. G., Galperin, Y. I., Zinin, L. V., Grigoriev, S. A., & Mendillo, M. (2002). Polarization jet events and excitation of weak sar arcs. *Geophysical Research Letters,* 29(12), 26-1–26-4. https://doi.org/10.1029/2001GL014388

Ogawa, Y., Kadokura, A., Ejiri, M. K. (2020), Optical calibration system of NIPR for aurora and airglow observations. *Polar Science*, Volume 26. https://doi.org/10.1016/j.polar.2020.100570

Ozaki, M., Shiokawa, K., Horne, R. B., Engebretson, M. J., Lessard, M., Ogawa, Y., et al. (2021). Magnetic conjugacy of Pc1 waves and isolated proton precipitation at subauroral latitudes: Importance of ionosphere as intensity modulation region. *Geophysical Research Letters,* 48, e2020GL091384. https://doi.org/10.1029/2020GL091384

Rees, M. H., and Roble, R. G. (1975). Observations and theory of the formation of stable auroral red arcs, *Reviews of Geophysics*, 13, 201.

Rostoker, G. Akasofu, S.I. Foster, J. et al. (1980). Magnetospheric substorm – Definition and signatures. *Journal of Geophysical Research*, (A4), 1663-1668

Smiddy, M., Kelley, M. C., Burke, W., Rich, F., Sagalyn, R., Shuman, B., Hays, R., and Lai, S. (1977). Intense poleward-directed electric fields near the ionospheric projection of the plasmapause, *Geophysical Research Letters,* 4, 543 –546.

Spiro, R. W., Heelis, R. A., and Hanson, W. B. (1979). Rapid subauroral ion drifts observed by Atmospheric Explorer C, *Geophysical Research Letters,* 6, 657 – 660.

Shiokawa, K., Katoh, Y., Satoh, M., Ejiri, M. K., Ogawa, T., Nakamura, T., Tsuda, T., & Wiens, R. H. (1999). Development of optical mesosphere thermosphere imagers (OMTI). *Earth, Planets and Space,* 51, 887–896. https://doi.org/10.1186/BF03353247

Shiokawa, K., Hosokawa, K., Sakaguchi, K., Ieda, A., Otsuka, Y., Ogawa, T., & Connors, M. (2009). The optical mesosphere thermosphere imagers (omtis) for network measurements of aurora and airglow. *AIP Conference Proceedings,* 1144(1), 212–215. https://doi.org/

10.1063/1.3169292

Shiokawa, K., Katoh, Y., Hamaguchi, Y., Yamamoto, Y., Adachi, T., Ozaki, M., et al. (2017). Ground-based instruments of the pwing project to investigate dynamics of the inner magnetosphere at subauroral latitudes as a part of the erg-ground coordinated observation network. *Earth Planets and Space,* 69(1), 160. https://doi.org/10.1186/s40623-017-0745-9

Sakaguchi, K., Shiokawa, K., Miyoshi, Y., Otsuka, Y., Ogawa, T., Asamura, K., & Connors, M. (2008). Simultaneous appearance of isolated auroral arcs and Pc 1 geomagnetic pulsations at subauroral latitudes. *Journal of Geophysical Research*, 113(A5), A05201. https://doi.org/10.1029/2007ja012888

Takagi, Y., Shiokawa, K., Otsuka, Y., Connors, M., & Schofield, I. (2018). Statistical analysis of SAR arc detachment from the main oval based on 11-year, all-sky imaging observation at Athabasca, Canada. *Geophysical Research Letters*, 45, 11,539–11,546. https://doi.org/10.1029/2018GL079615

Yadav, S., Shiokawa, K., Otsuka, Y., Connors, M., and St. Maurice, J.-P. (2021a), Multi-wavelength imaging observations of STEVE at

Athabasca, Canada. *Journal of Geophysical Research: Space Physics*, 125, https://doi.org/10.1029/2020JA028622.

Yadav, S., Shiokawa, K., Oyama, S., Inaba, Y., Takahashi, N., Seki, K., et al. (2021b), Study of an equatorward detachment of auroral arc from the oval using ground-space observations and the BATS-R-US – CIMI model. Under second review in *Journal of Geophysical Research: Space Physics*.

Zhou, S., Luan, X., Burch, J. L., Yao, Z., Han, D. S., Tian, C., et. al. (2021), A possible mechanism on the detachment between a subauroral proton arc and the auroral oval. *Journal of Geophysical Research: Space Physics,* 126, e2020JA028493. https://doi.org/10.1029/2020JA028493